1. FINAL SCIENTIFIC TECHNICAL REPORT

Report Title:

Extreme Environment Silicon Carbide Hybrid Temperature & Pressure Optical Sensors

Type of Report: FINAL

Reporting Period Start Date: July 1, 2007

Reporting Period End Date: Sept 30, 2010.

Principal Author: Nabeel A. Riza

Date Report Was Issued: December 3, 2010.

DOE Award No.: DE-FG26-07NT43068

Name & Address of Submitting Organization:

University of Central Florida

CREOL, College of Optics & Photonics

4000 Central Florida Blvd.,

Orlando, FL 32816-2700.

2. Abstract

This final report contains the main results from a 3-year program to further investigate the merits of SiC-based hybrid sensor designs for extreme environment measurements in gas turbines. The study is divided in three parts. Part 1 studies the material properties of SiC such as temporal response, refractive index change with temperature, and material thermal response reversibility. Sensor data from a combustion rig-test using this SiC sensor technology is analyzed and a robust distributed sensor network design is proposed. Part 2 of the study focuses on introducing redundancy in the sensor signal processing to provide improved temperature measurement robustness. In this regard, two distinct measurement methods emerge. A first method uses laser wavelength sensitivity of the SiC refractive index behavior and a second method that engages the Black-Body (BB) radiation of the SiC package. Part 3 of the program investigates a new way to measure pressure via a distance measurement technique that applies to hot objects including corrosive fluids.

3. Table of Contents

1. Final Report Title Page	1
2. Abstract	2
3. Table of Contents	3
4. Executive Summary	4
5. Experimental Methods	6
6. Results and Discussion	17
7. Conclusion	44
8. References	46

4. Executive Summary

This final report contains the main results from a 3-year program to further investigate the merits of SiC-based hybrid sensor designs for extreme environment measurements in gas turbines [1-6]. The study is divided in three parts. Part 1 studies the material properties of SiC such as temporal response, refractive index change with temperature, and material thermal response reversibility. Specifically, Single crystal 6H-SiC chips and support infrastructure provided by Nuonics, Inc. have been used in a new study to characterize the refractive index and rate of change of refractive index with temperatures up-to 1077 ^{o}C. New data compared to prior works reveals interesting non-linear thermal behavior of 6H-SiC. These conducted experiments and calculations show that at temperatures greater than about 550 ^{o}C, the TOC of single crystal 6H-SiC changes little and essentially becomes constant near 8 x 10^{-5} / ^{o}C. In effect, the optical power cycles have near constant periods as temperature exceeds about 550 ^{o}C. New data has been measured on the temporal response of single crystal SiC due to thermal heating via a thermal step function. Specifically, the newly conducted experiments and calculations show that the instantaneous temporal response of a 400 micron thick 1 cm x 1 cm square single crystal SiC chip when subjected to a conductive temperature step function of 90 deg-C peak value is under 1/30 seconds. Given the 1 mm diameter conductive heat tip placed on the chip, ~ 16 seconds are required to reach the steady state 90 deg-C temperature of the heat tip from the 25 deg-C room temperature setting. Approximately the same time (~ 17 seconds) is required for the chip to cool down to steady state room temperature by simply using convection cooling, indicating a reversible and repeatable heat/cool refractive index change process for the observed temperature range. Sensor data from a combustion rig-test using this SiC sensor technology is analyzed and a robust distributed sensor network design is proposed. A design and assembly study has been conducted to realize a dedicated portable optical transceiver module that allowed testing of the new hybrid all-SiC sensor probe from room temperature to 1000°C in the laboratory and also in a combustion rig field setting. Experimental results showed the robustness of the sensor to mechanical misalignments of the probe assembly that can otherwise cause sensor malfunction. Turbine rig test raw sensor data, including thermal shock on flame ignition has been initially analyzed and compared to Thermo-Couple (TC) temperature readings. The conducted analysis indicates that the TC temperature reading temporal response is similar to the demonstrated single crystal 6H-SiC temperature sensing probe.

Part 2 of the study focuses on introducing redundancy in the sensor signal processing to provide improved temperature measurement robustness. In this regard, two distinct measurement methods emerge. A first method uses laser wavelength sensitivity of the SiC refractive index behavior and a second method that engages the Black-body radiation of the SiC package. A new method to derive coarse temperature of a single crystal 6H-SiC probe has been tested successfully to over 1000 deg-C. This method can provide unambiguous temperature readings. Furthermore, a novel signal processing approach has been designed and demonstrated for the single crystal 6H-SiC temperature sensing probe

that can deliver both high dynamic range and high resolution temperature sensing using wavelength sensitive data acquisition. The specific refractive index behavior of SiC with temperature allows spectral width measurement and peak shift processing that provides independent coarse and fine temperature measurements, respectively. An alternate method via the rig test indicates that pyrometry (or SiC package BB radiation measurement) combined with laser interferometry can also be used to measure extreme temperatures, and this aspect has been demonstrated to 1000 deg-C.

Part 3 of the program investigates a new way to measure pressure via a distance measurement technique that applies to hot objects including corrosive fluids. Using an electronically controlled lens and measuring the spatial size of the reflected light off the sensing zone (i.e., SiC chip or liquid level), the physical motion of the sensing layer due to pressure,etc, and be accurately measured using a non-contact laser beam.This modified level measurement sensor has been designed and tested for lab. demonstrations towards realization of an all-SiC pressure sensor technology based on remote laser beam distance measurements. The optical physics of this modified sensor has been experimentally verified via optical beam camera views so it can be applied to liquid level measurements in advanced high efficiency power plant gas turbines. Tests have been done with both solid object motion and liquid level motions.

5. Experimental Methods

5.1 Part 1 of Program

Part 1 studies the material properties of SiC such as temporal response, refractive index change with temperature, and material thermal response reversibility. Specifically, Single crystal 6H-SiC chips and support infrastructure provided by Nuonics, Inc. have been used in a new study to characterize the refractive index and rate of change of refractive index with temperatures up-to 1077 ^{o}C.

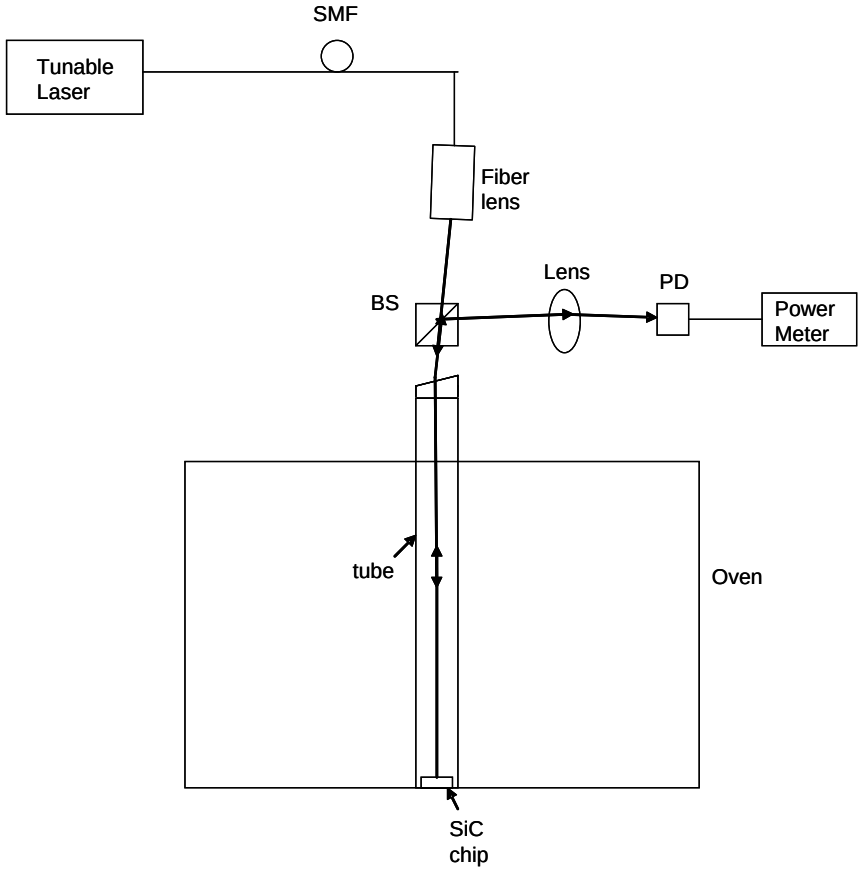

Fig. 5.1.1. Experimental setup to measure power reflected off a SiC chip placed in an oven from 685 ^{o}C to 1077 ^{o}C.

Fig. 5.1.1 shows the experimental setup used to measure the reflected power off a SiC chip placed in an oven as the oven temperature is raised to 1077 ^{o}C. Light from a tunable IR source is launched towards the SiC chip using a fiber lens. This light is slightly deflected from the window and hits the SiC chip at near normal incidence. The light reflected off the SiC chip is then deflected off a beam-splitter and focused onto a large area photo-detector using a lens. This optical power is measured using a power-meter.

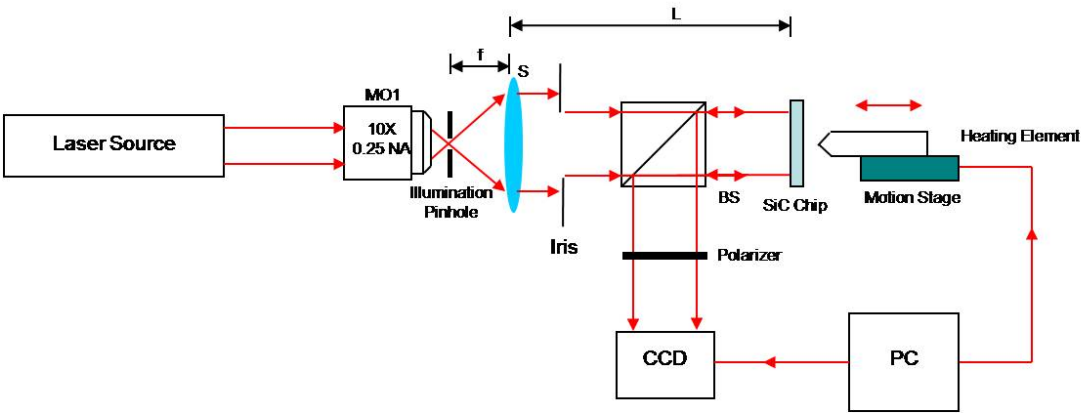

Fig. 5.1.2 Optical system design used for measuring the temporal response of the SiC chip as its temperature is changed using a conducting thermal step function induced by a pointed heating element moved by a computer controlled actuator. MO: Micro-objective, S: Spherical lens, BS: Beam Splitter.

Figure 5.1.2 shows the experimental setup used to measure the temporal response of a 400 μm thick SiC chip such as used in the Nuonics designed probe when a 1 mm diameter heating element is brought in contact with the chip. Light from a 633 nm He-Ne laser is collimated using a 10x micro-objective lens together with a 15 cm focal length spherical lens. The collimated light is retro-reflected off the SiC chip held vertically in a thermally insulating holder. This retro-reflected light from the heated SiC chip is imaged onto a CCD camera forming the chip characteristic interferogram. The diameter of the collimated beam is set at 5 mm using an iris and is smaller than the 8 mm x 8 mm exposed surface of the chip. The deployed SiC chip has a slit wedge effect, hence producing the desired interferogram with linear optical fringes that can be observed with a camera. The heating element is mounted on a motorized digital-step translational stage. Computer based control allows the heating element to move in a digital step so as to make a one step physical contact with the SiC chip when computer actuated. One continuously monitors the interferogram on the CCD.

The proposed all-SiC probe technology can form a highly efficient distributed temperature sensing system for a gas turbine. In the proposed distributed sensor system shown in Fig. 5.1.3, one is using 16 of our proposed all-SiC front-end probe hybrid temperature sensors. The fibers terminate well before the hot zones external to the combustor, letting the wireless light to make the final connection with the hot SiC chip at the tip of the inserted probe deep within the combustor. In such as way, N=16 all-passive temperature probe sticks are inserted at various points around the combustor in an advanced turbine system, all interconnected through a low loss 1XN optomechanical/MEMS-type optical switch with a typical 1 ms individual sensor access time. Because the remoted frontend probe sensors are all designed with the same SMF interconnection channel for both light transmit and light receive operations, the entire distributed sensor control system efficiently uses one low 10 mW power tunable laser, one optical power meter, and one optical circular to complete the full control system. This design feature of the proposed system not only saves system cost, power, weight,

and size, it also prevents unnecessary exposure of alternate receiver optics such as Beam Splitters, optical cameras, etc, to the industrial environment near a gas turbine combustor inlet. Ultimately, one can envision N=100 temperature sensors using the proposed networked control system design.

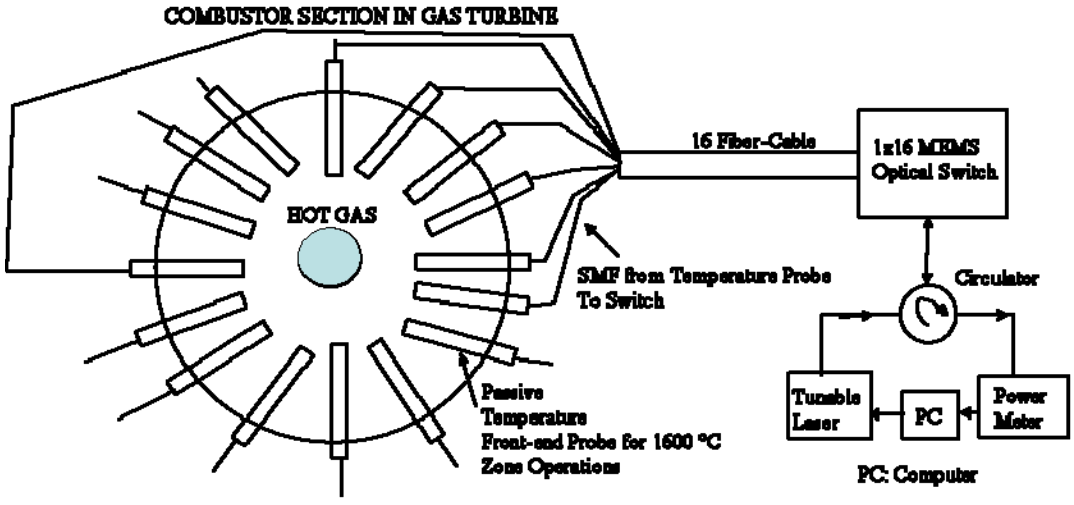

Fig. 5.1.3 Implemented design of the distributed fiber-optic sensor network for gas turbine temperature sensing using the all-SiC hybrid design temperature sensing probes.

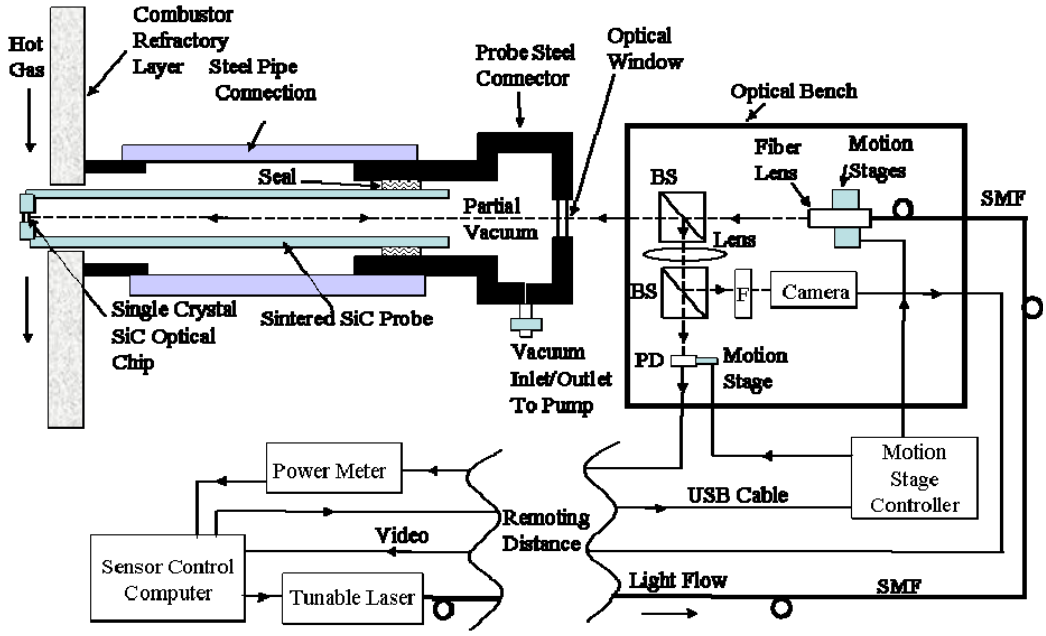

Fig. 5.1.4 All-SiC frontend probe-based optical sensor system for extreme gas temperature measurements in combustion engines.

Fig. 5.1.4 shows the basic research design and method of the proposed all-SiC frontend probe sensor system used for extreme gas temperature measurement within the combustor section of a gas turbine courtesy of Nuonics, Inc. with facility support from Siemens. The system is sub-divided into three thermally isolated sub-systems forming a hybrid optical design engaging both wired and wireless optics. The first sub-system represents the sensor controls and processing station that is remotely located at a safe site for human interface. This sub-system includes the sensor control computer, optical power meter, and tunable laser. The remoting distance depending on the electrical signal drive requirements and can range from tens of meters to near a hundred meters. The second sub-system consists of the optical transceiver module containing targeting light beam and detection optics, active mechanics, and electronics. This transceiver module is located in close proximity (e.g., a few cm) from the frontend probe that forms the third sub-system that is uniquely passive, i.e., contains no lasers, detectors, electronics, or other electrically controlled device. The physical link between the controls sub-system and the transceiver sub-system is via one Single Mode Fiber (SMF) optical cable and three electrical (USB style) cables, providing significant environmental isolation between the two sites. More importantly, the hot frontend probe sub-system is thermally decoupled from the transceiver sub-system with the only physical connection established via a single wireless optical link interfacing the hot SiC optical chip with the laser beam emerging from the SMF-coupled Fiber Lens (FL). The transceiver module is preferably enclosed in an environmentally protected chamber to minimize moisture, dust, and air currents. The transceiver module is designed for under 70 ºC operation that is ideally compatible with turbine manufacturer external safety and technician operational environment requirements. Furthermore, this friendly < 70 ºC temperature range is also compatible with temperature limits for standard fiber-optics, mechanics, and electronics. The transceiver module is mechanically interfaced to a thermally isolated cooler part of the turbine housing. The frontend probe sub-system consists of a steel connector that forms a pressurized fitting at the inlet to the engine combustor section where gas temperature sensing is desired. This steel connector via a high temperature pressure seal connects to a long all-SiC probe that extends slightly into the hot gas section of the combustor. At the tip of this probe is embedded a thick single crystal SiC optical chip packaged within the sintered SiC material thus forming the much desired CTE-matched frontend.

5.2 Part 2 of Program

Fig.5.2.1 shows the proposed temperature sensor system with a 6-H single crystal SiC chip as the sensing element within an all-SiC probe. The SiC chip acts as a classic FP etalon with reflectance given by:

$$R_{FP} = \frac{R_1 + R_2 + 2\sqrt{R_1 R_2}\cos\varphi}{1 + R_1 R_2 + 2\sqrt{R_1 R_2}\cos\varphi}. \qquad (1)$$

Here $\varphi = \frac{4\pi}{\lambda} n(\lambda, T) t(T)$ where n(λ,T) is the chip refractive index at wavelength λ and chip temperature T, t(T) is the chip thickness at temperature T, and R_1 and R_2 are

the classic Fresnel Power coefficients for the SiC-air interface given by $R_1=R_2= [(1-n)/(1+n)]^2$.

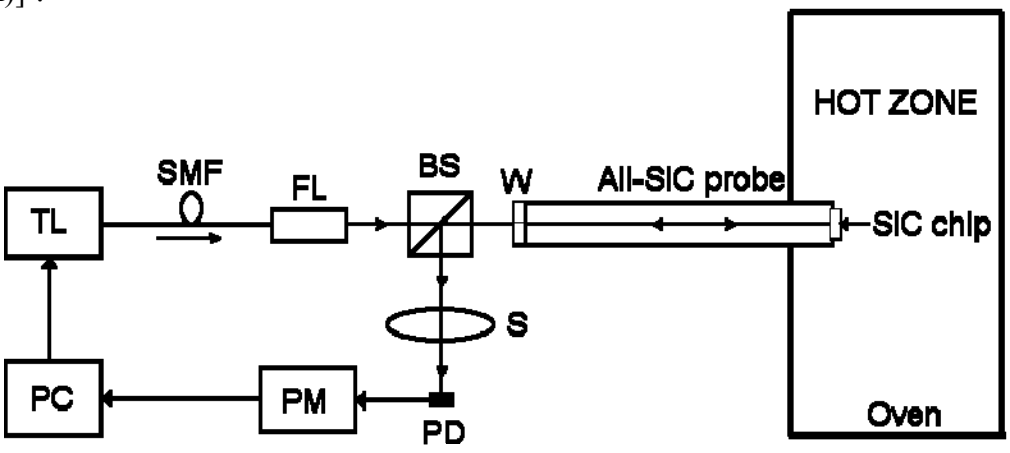

Fig. 5.2.1. All-SiC probe hybrid wireless-wired optical sensor for extreme temperature measurements. TL: Tunable Laser; SMF: Single-Mode Fiber; FL: Fiber Lens; BS: Beam Splitter; W: Optical Window; S: Spherical Lens; PD: Photo-Detector; PM: Power Meter; PC: Personal Computer.

As previously demonstrated in our work, the wavelength difference $\Delta\lambda$ between k consecutive maximas or minimas in the optical spectrum of the SiC FP etalon is temperature dependent and is given by:

$$\Delta\lambda = \frac{k}{2t\left[\frac{BC}{n_1\left(\lambda_1^{\,2} - C\right)^2} + \frac{n_1}{\lambda_1^{\,2}}\right]} . \qquad (2)$$

where the Sellmeier coefficients are B = 5.5515 and C = $0.026406\text{x}10^{-12}$, and n_1 is the temperature-dependent refractive index of SiC at wavelength λ_1 and t is the temperature-dependent thickness of the SiC optical chip. By measuring $\Delta\lambda$, a coarse value of the SiC chip temperature can be found from the $\Delta\lambda$ against temperature curve. From Eq.1, the SiC FP etalon optical spectrum has maximas located where $\cos(\varphi) = 1$. This condition can be re-written as:

$$\frac{4\pi}{\lambda_{peak}} n\left(\lambda_{peak}, T\right) t(T) = 2m\pi , \qquad (3)$$

where m = 1,2,…...,M. The change in refractive index due to wavelength for SiC can be expressed as:

$$\Delta n \approx \frac{-\lambda BC}{n\left(\lambda^2 - C\right)^2}\Delta\lambda \quad . \qquad (4)$$

Using Eq.4, one can write Eq.3 in terms of the already known refractive index n_1 at wavelength λ_1 as:

$$\lambda_{peak} = \frac{\frac{2t}{m}\left[n_1 + \frac{\lambda_1^{\,2} BC}{n_1\left(\lambda_1^{\,2} - C\right)^2} \right]}{1 + \frac{2t\lambda_1 BC}{mn_1\left(\lambda_1^{\,2} - C\right)^2}}, \qquad (5)$$

Eq. 5 gives the temperature-dependent maxima locations of the SiC FP etalon optical spectrum. The location of a specific peak of this optical spectrum can be used to accurately and unambiguously determine the temperature of the SiC chip within one FSR of the FP etalon. This technique can be combined with the coarse measurement technique from Eq.2 to simultaneously determine temperature with a high resolution and over a wide range. To determine a given temperature, first a $\Delta\lambda$ value can be measured that gives a coarse value of the temperature based on a previously calibrated $\Delta\lambda$ against temperature curve. The k-value for this measurement needs to be sufficiently high in order to determine the temperature up to one unambiguous temperature zone for the FP etalon peak shift technique. Once the unambiguous temperature zone is identified, then the wavelength peak location λ_{peak} within one FSR of an arbitrarily chosen wavelength λ_c can be used to give a precise value for the temperature, again based on a previously calibrated λ_{peak} against temperature curve.

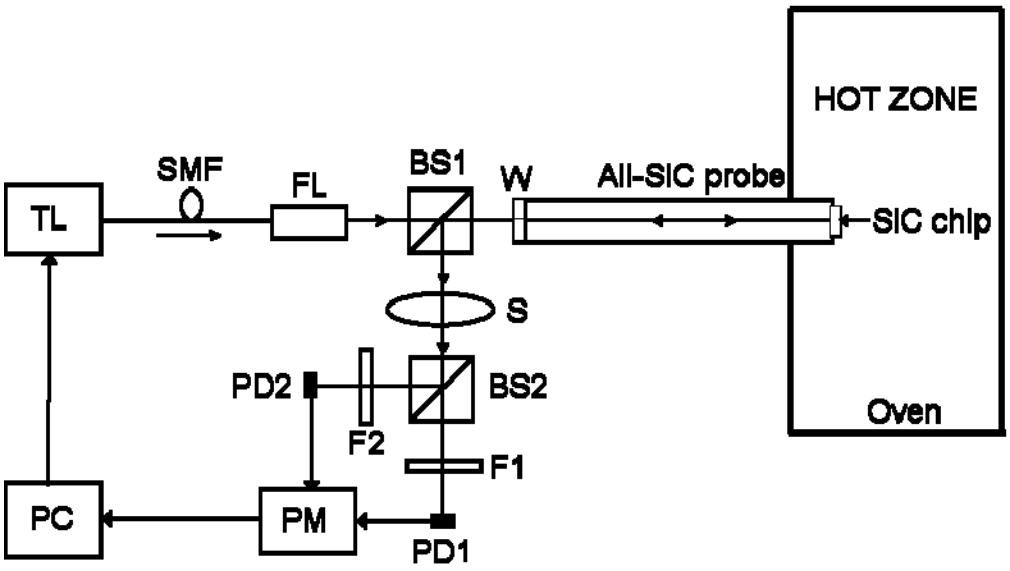

Fig. 5.2.2. Proposed high resolution extreme environment temperature sensor. SMF: Single-Mode Fiber; PC: Personal Computer.

Fig. 5.2.2 shows the proposed sensor design. For coarse temperature measurement, the SiC chip is used as a BB radiator in a two-color pyrometer configuration. The spectral radiance of an ideal BB radiator is given by Planck's law:

$$I(\lambda, T) = \frac{2hc^2}{\lambda^5} \frac{1}{e^{\frac{hc}{\lambda kT}} - 1}. \qquad (6)$$

λ is the emitted radiation wavelength, T is the BB temperature in Kelvins, h is the Planck's constant, c is the speed of light, and k is the Boltzmann's constant. In addition to radiation emitted from the SiC chip, background radiation caused by stray furnace light or another heat source is also detected by the photo-detectors. One can assume that the SiC chip and the background radiation source are at the same temperature as SiC has a high (e.g., 120 W/m.K) thermal conductivity. Hence using Eq.6 under the Wein approximation (i.e., hc>>λkT), the ratio of output detected BB radiation powers at the two wavelengths of interest λ_1 and λ_2 is given by:

$$R = \frac{P_{\lambda_1}}{P_{\lambda_2}} = A_S \left(\frac{\lambda_2}{\lambda_1} \right)^5 \frac{\varepsilon(\lambda_1, T) + a(\lambda_1, T)}{\varepsilon(\lambda_2, T) + a(\lambda_2, T)} \exp\left[-C_2 \left(\frac{1}{\lambda_1} - \frac{1}{\lambda_2} \right) \frac{1}{T} \right]. \qquad (7)$$

A_S is a sensor-specific constant that takes into account spectral transmittance of the optical sensor system, spectral response and the bandwidth of the optical filters F1 and F2, and the responsivity of the photo-detectors PD1 and PD2. ε(λ,T) is the specific emissivity of SiC, a(λ,T) is the product of the emissivity of the background radiation source and its transmission percentage through the system and C_2 = hc/k. The emissivities also have a weak dependence on λ provided there are no sharp emission lines near either of the two working wavelengths. If the two wavelengths are selected close to each other, then the effect of ε on the ratio is minimal and Eq.7 can be written as:

$$\ln R = \alpha + \frac{\beta}{T}. \qquad (8)$$

α and β are constants that can be determined by sensor calibration. Once α and β are determined, a coarse value of temperature can be determined by measuring the ratio R and finding the corresponding value of T from the calibrated R against T curve. For fine temperature measurement, the SiC chip is used as a FP etalon with reflectance given by:

$$R_{FP} = \frac{R_1 + R_2 + 2\sqrt{R_1 R_2}\cos\varphi}{1 + R_1 R_2 + 2\sqrt{R_1 R_2}\cos\varphi}. \qquad (9)$$

R_1 and R_2 are the classic Fresnel Power coefficients for the SiC-air interface given by $R_1=R_2= [(1-n)/(1+n)]^2$ and $\varphi=(4\pi/\lambda)\ n(T)t(T)$. At temperature T, n(T) is the chip refractive index at laser wavelength λ and t(T) is the chip thickness. The reflected laser power P(λ, T) is proportional to R_{FP} and has a sinusoidal behavior with φ. The change in P due to change in λ can be written as:

$$\frac{dP}{d\lambda} = \frac{dP}{d\varphi}\frac{d\varphi}{d\lambda} = -\frac{4\pi}{\lambda^2} n(T) t(T) \frac{dP}{d\varphi}. \qquad (10)$$

Eq.10 implies that if dP/dλ is positive, i.e., the reflected power increases with an increase in wavelength, then dP/dφ would be negative and vice versa. The normalized SiC chip reflected laser light power P_{norm} is given by:

$$P_{norm} = \frac{P - P_{\min}}{P_{\max} - P_{\min}}. \qquad (11)$$

P_{max} and P_{min} are the localized maximum and minimum power values. To determine a given T, first the two-color pyrometer is used to find a coarse value of temperature within one 2π cycle (alternatively referred to as a coarse bin) of the P_{norm} against φ curve. Next, within that P_{norm} cycle (or coarse bin), the normalized reflected power is measured at a

fixed laser wavelength $\lambda = \lambda_L$ along with the sign of the change in detected power with change in λ.

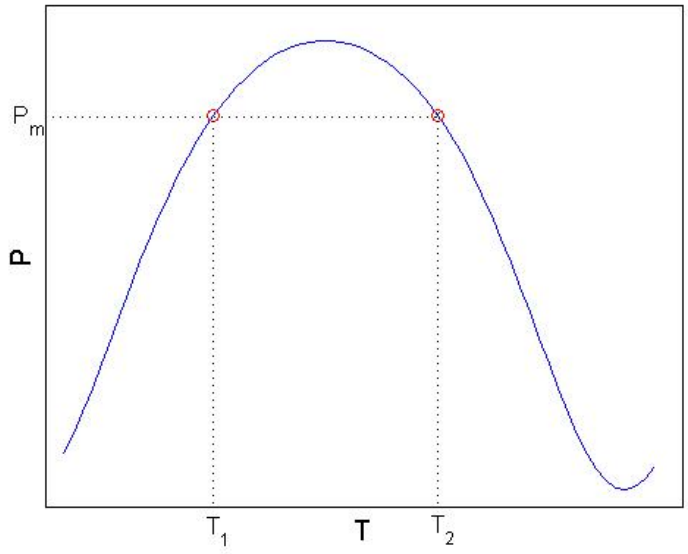

(a)

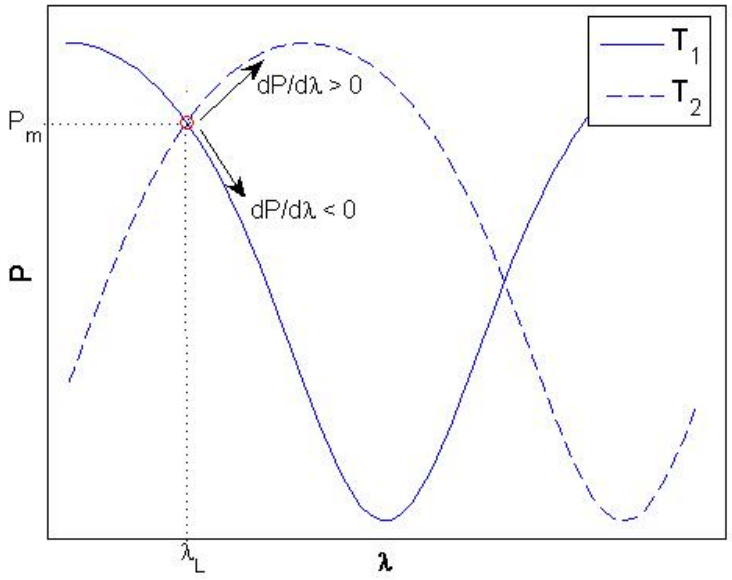

(b)

Fig. 5.2.3. (a) A graphical display showing that at a given temperature, the measured optical power reading P_m within a coarse bin indicates two temperatures values of T_1 and T_2 and only one of them is the true temperature. (b) A graphical display of the slope or $dP/d\lambda$ sign measurement working principle for selecting either T_1 or T_2 as the unambiguous temperature for the proposed sensor.

Specifically, Fig.5.2.3.(a) shows that at a given temperature, the measured optical power reading P_m within a coarse bin indicates two temperatures values of T_1 and T_2. Given that only one of them is the true temperature, there is a two state ambiguity problem within a coarse bin. Fig. 5.2.3(b) shows via a graphical display as to how the slope or $dP/d\lambda$ sign measurement is used for selecting either T_1 or T_2 as the true unambiguous temperature for the proposed sensor. The exact value of T can then be found from a previously calibrated P_{norm} against T curve at λ_L .

5.3 Part 3 of Program

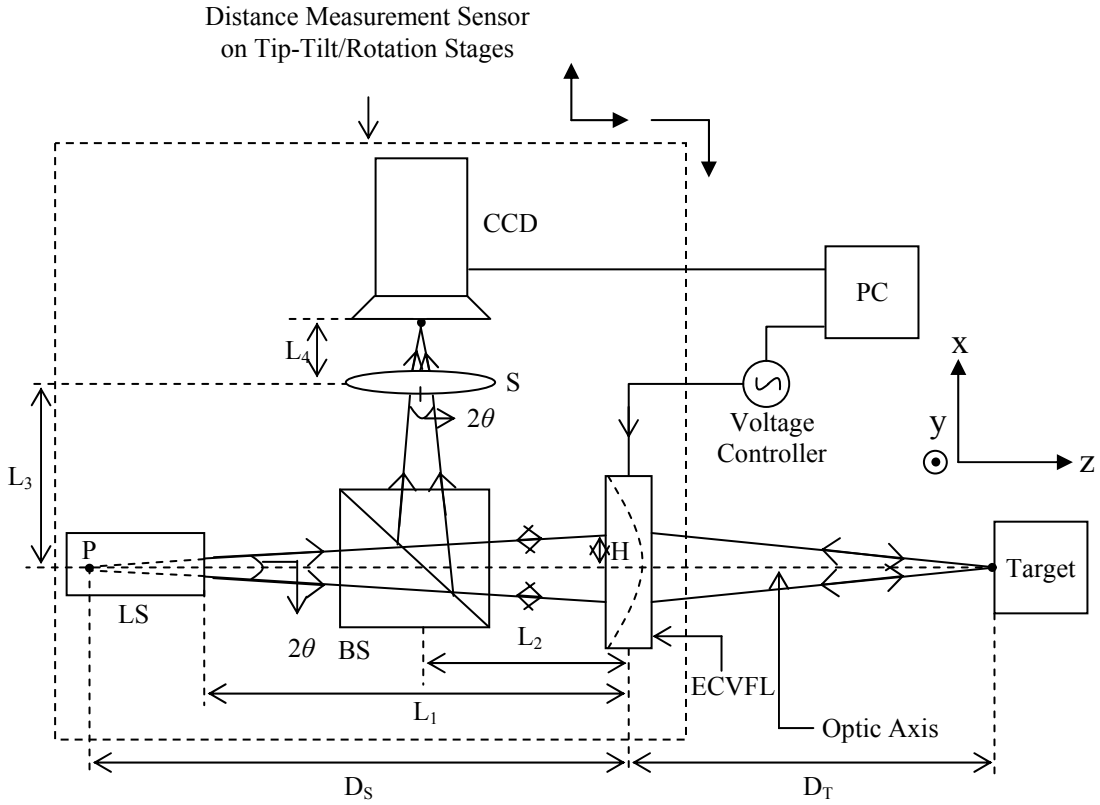

Fig.5.3.1 Proposed level/pressure measurement sensor using spatial signal processing that can be applied via the prior all-SiC frontend probe-based optical sensor system for level measurements in combustion engines. The target represents for example the varying level interface.

Fig.5.3.1 shows the proposed level measurement sensor that can also be designed as a pressure sensor using a laser beam as the source of spatially controlled energy directed towards a target under distance/level/pressure measurement. In this case, the target is optically reflective (shown as a mirror) over the interrogated region, allowing a return laser beam to enter the receive section of the sensor Transmit-Receive (T-R) module that includes tip/tilt, rotation, and translational motion stages for proper alignment. The target can also be an optically diffused target and in this case direct off-axis viewing of the target by a camera is required. Light from a Laser Source (LS) passes

through a Beam Splitter (BS) to enter the ECVFL than in-turn electronically produces a laser beam with different far-field focused positions in time. The target reflected beam retraces the transmit beam path to pass via the ECVFL to strike the BS to be deflected towards a focusing lens S to eventually fall on a Two Dimensional (2-D) Charge-Coupled Device (CCD). As the focal length F of the ECVFL is swept over a given range, the laser spot formed on the target and also observed on the CCD sweeps over various sizes.

When the CCD and equivalently the target observed spot is at a spatial size minimum, one deduces that the ECVFL is set to the optimal focal length F for target distance measurement. As the sensor module design parameters are known such as distances between the various optical components, laser beam radius H on the ECVFL, laser beam divergence half-angle θ in radians, S lens focal length F_s, and ECVFL focal length F for the specific target at minimum spot size condition, one can use ray optics or geometry to compute the target distance D_T. The ECVFL performs the thin-lens imaging operation between the target plane and the back-projected laser virtual point source P seen inside LS. Hence when the target is in the proper focused imaging state with the ECVFL set to optimal F, the lens imaging condition:

$$D_T = D_S F \Big/ (D_S - F) \quad , \qquad (1)$$

is obeyed. Here D_S is the distance between point P and the ECVFL and by geometry $D_S = H/(\tan\theta)$. For a given sensor design, the computed D_S is used with the lens imaging formula and the optimal F for the illuminated target to compute D_T. For the sensor distance/level measurement range $D_{T\text{-max}}$ - $D_{T\text{-min}}$, one again uses the imaging lens formula with the ECFVL minimum F_{min} and maximum F_{max} focal lengths possible to compute the minimum $D_{T\text{-min}}$ and maximum $D_{T\text{-max}}$ target distances, respectively. The resolution of the sensor at a target distance D_T is given by:

$$\Delta D_T = \left(\frac{dD_T}{dF} \right) \Delta F \quad , \qquad (2)$$

where using the imaging condition, the derivative

$$\frac{dD_T}{dF} = \frac{(D_S - F)D_S + D_S F}{(D_S - F)^2} \quad , \qquad (3)$$

The smallest possible change ΔF in F is related to the smallest possible change ΔV_c in the applied voltage V_c to the ECVFL. As a typical ECVFL can have different F versus V_c regimes of operation, ΔF will be different for the same voltage change given a different absolute voltage V_c required to set the ECVFL to specific focal length F for a given target distance D_T. From optical layout symmetry conditions shown in Fig.5.3.1, the lens S should be placed such that $L_3 = L_1 - L_2$, where L_1 is the distance between the ECVFL and laser exit aperture, L_2 is the distance between the BS center and ECVFL, and L_3 is the distance between the BS center and S. With no S present, the converging rays coming from ECVFL and BS come to a focus forming an image point at a distance of D_S from ECVFL. In effect, at the S location one can estimate the existence of a virtual converging lens S_v with a focal length $F_v = D_s - L_1$. As F_v can be rather long, one can place a real converging lens S to shorten the distance L_4 between the CCD and S. In this case using the cascading formula for two thin lenses S and S_v, the equivalent focal length distance L_4 can be computed from:

$$\frac{1}{L_4} = \frac{1}{F_V} + \frac{1}{F_S}. \qquad (4)$$

Thus the distance L_4 computed from Eqn.4 ensures that ones get the minimum spot size at the target and the CCD at the same time.

Fig.5.3.2 shows the proposed liquid level sensor using an Electronically Controlled Variable Focus Lens (ECVFL). A low power Laser Source (LS) forms a directed optical beam that passes through a Beam Splitter (BS), a ECVFL, and an optional mirror M to actively illuminate a small zone on the liquid surface. The liquid is enclosed in a window sealed tank suitable for large volume storage of hazardous liquids.

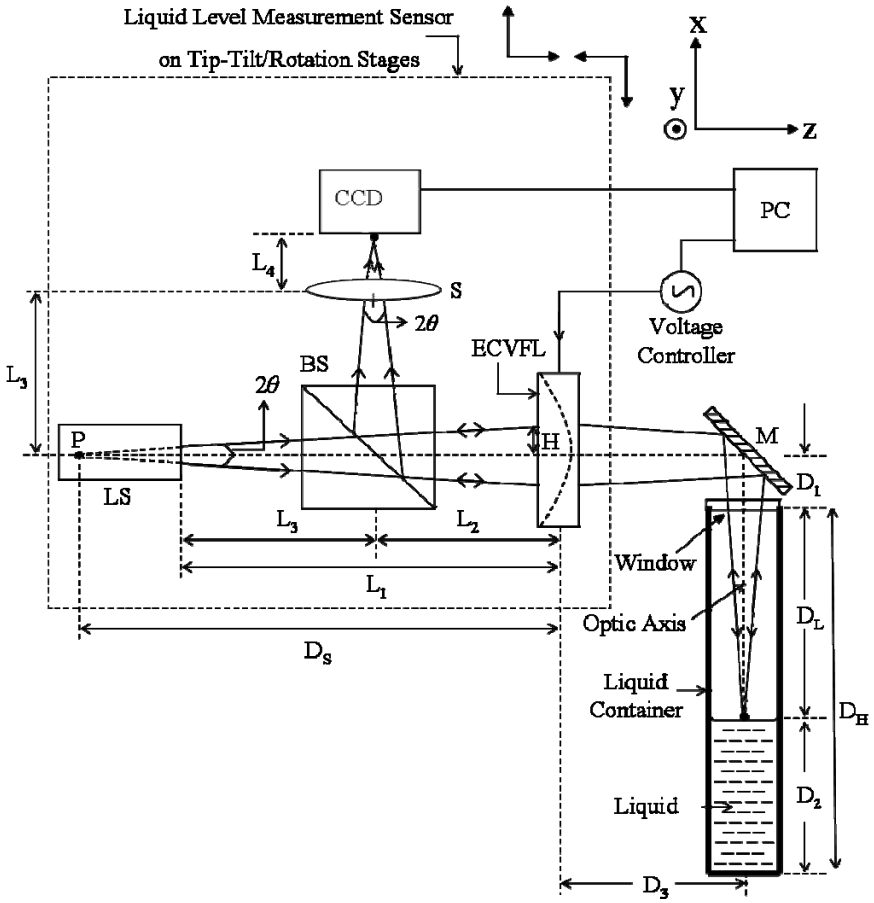

Fig.5.3.2 Proposed liquid level sensor using spatial signal processing. (b) Sensor laser beam agile focus operation set for liquid depth level A reading corresponding to smallest liquid

The light reflected off the liquid surface retraces the transmit beam path and is deflected by the BS to pass through a lens S to fall on an optical detector chip such as a Charge Coupled Device (CCD). The sensor transceiver module is mounted on tip/tilt and rotation stages for optimizing optical alignment with the liquid in the tank. For optimal on-axis reflection, the Liquid Under Test (LUT) should form an optically smooth partially

reflective surface at the laser wavelength λ_L. In the event that the LUT is unable to form an adequate optically smooth surface for on-axis reflection, off-axis viewing of the LUT scattered light surface is engaged using an optical camera also placed in the modified transceiver module. The refractive index of the liquid n_L and the refractive index n_G of the non-liquid region (e.g., filled with air, nitrogen or simply vacuum) provides a measure of the liquid-gas interface reflectivity via the normal incidence Fresnel optical power reflectivity coefficient $R_F = [(n_L - n_G)/(n_L + n_G)]^2$. The values of R_F, liquid optical absorption coefficient at λ_L, and the maximum and minimum liquid volume levels in the tank determines what maximum laser power can be safely used for measurement given some light absorption is expected in the liquid.

6. Results and Discussions

6.1 Part 1 of Program

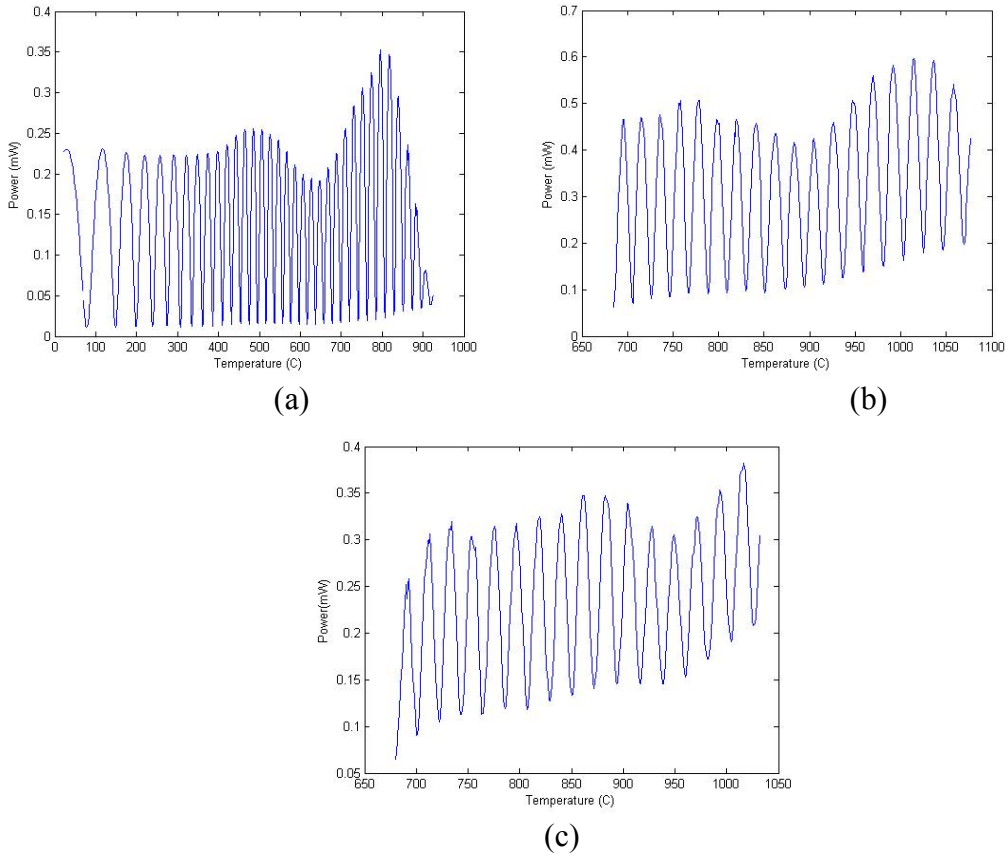

Fig. 6.1.2. Raw power data measured using the photo-detector as a function of oven temperature. (a) 22 – 925 ^oC, λ = 1560 nm (b) 685 – 1077 ^oC, λ = 1560 nm (c) 689 – 1032 ^oC, λ = 1575 nm.

Fig. 6.1.2(a) shows the raw power measured using this experimental setup as the temperature of the oven is raised from room temperature to 925 ^{o}C. Fig. 6.1.2(b) and (c) show the raw power measured for 685 ^{o}C to over 1000 ^{o}C for two different wavelengths λ = 1560 nm and λ = 1575 nm, respectively. This data is then processed to calculate the cosine of the instantaneous phase difference between the incident and the reflected beams as a function of temperature. The results are shown in Fig. 6.1.3.

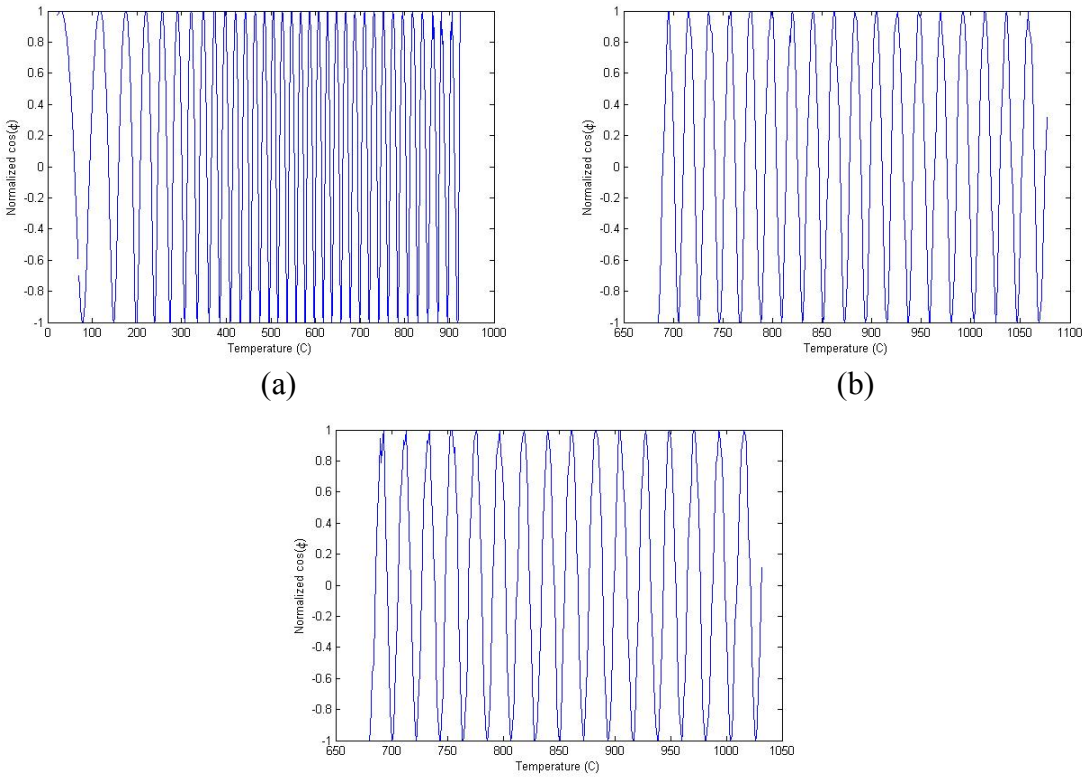

Fig. 6.1.3. Processed normalized cosine phase data as a function of oven temperature.

Taking the inverse of the Fig. 6.1.3 data and adding 2πm to each successive cycle, the unwrapped phase is calculated (see Fig. 6.1.4).

The thickness of the chip as a function of temperature is given by:

$$t(T) = [1 + \alpha \Delta T] t(T_i)$$

The calculated values for thickness as a function of temperature are shown in Fig. 6.1.5.

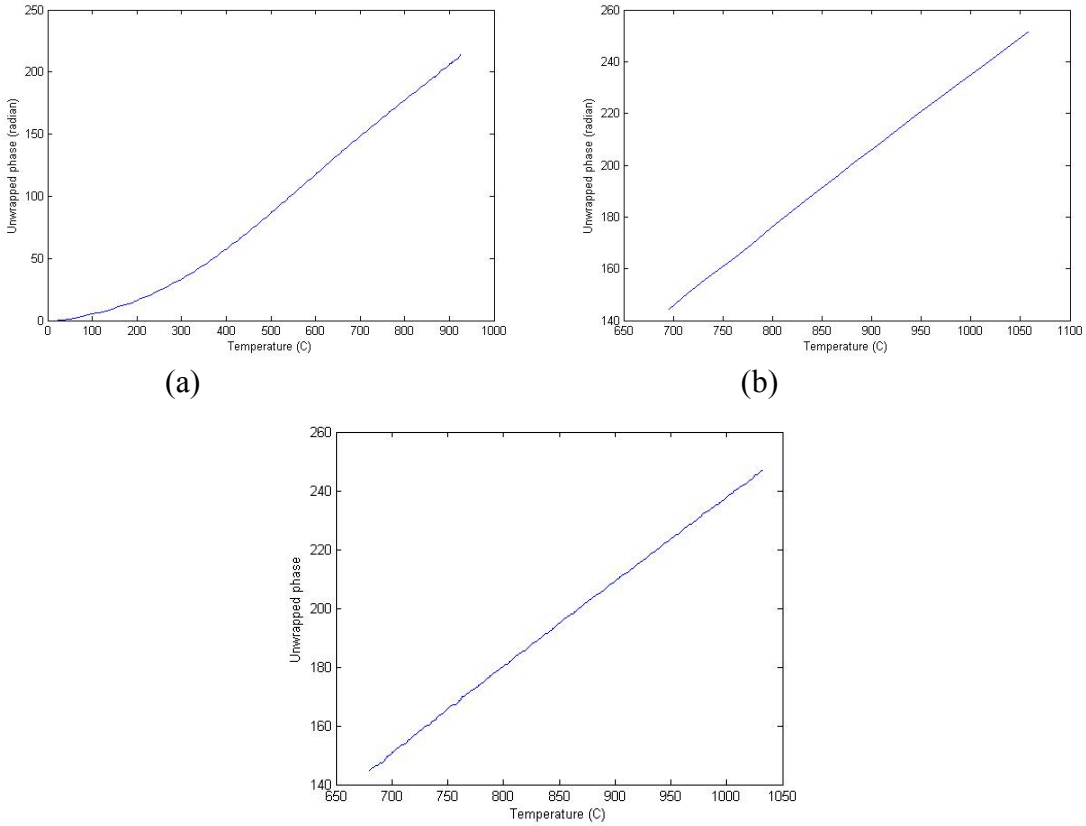

Fig. 6.1.4. Unwrapped phase data as a function of oven temperature.

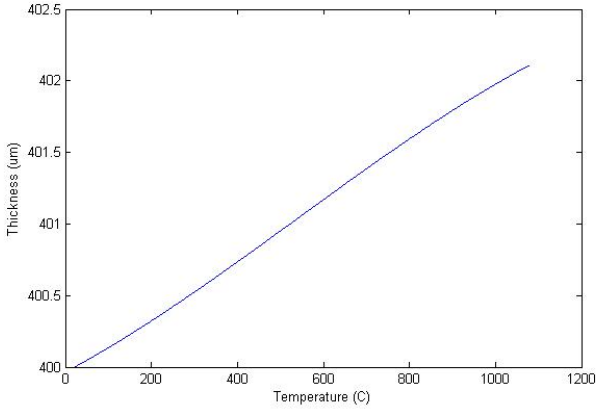

Fig. 6.1.5. Thickness of SiC chip as a function of temperature.

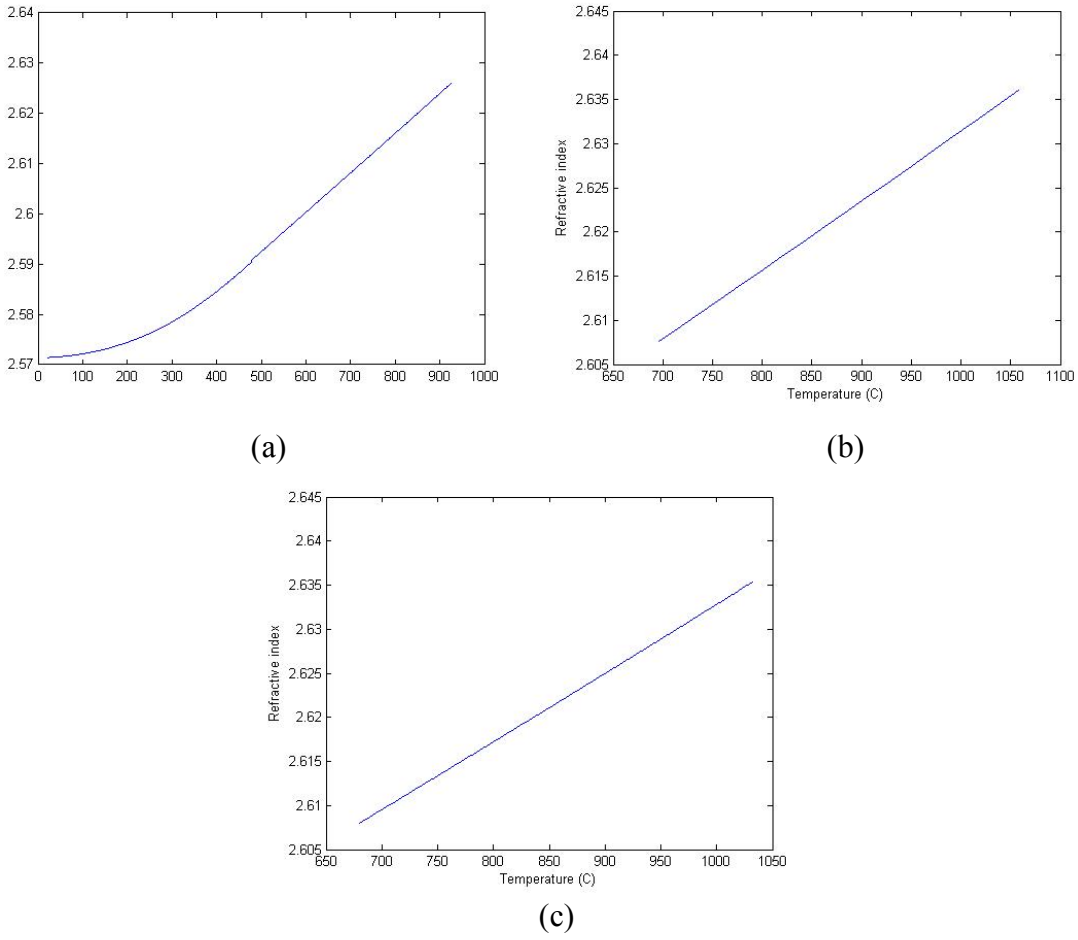

Fig. 6.1.6. Refractive index as a function of oven temperature.

The refractive index n_1 as a function of temperature is calculated from the unwrapped phase data and the thickness of the chip as follows:

$$n(T) = \frac{\Delta\phi(\Delta T)\lambda}{4\pi t(T)} + \frac{n(T_i)t(T_i)}{t(T)}$$

These computed values for the three different sets of data are shown in Fig. 6.1.6. Now, the TOC can simply be computed using:

$$TOC = \frac{1}{t(T)}\left(\frac{\lambda}{4\pi}\frac{d}{dT}[\phi(T)] - n(T)\alpha t(T_i)\right)$$

Here, we need an expression for the unwrapped phase φ(T) in order to calculate its derivative with respect to T. In our previous approach (see N. A. Riza, et.al., J. Appl. Phys, 98, 1, 2005), we used one third-order polynomial to fit the entire unwrapped phase data from room temperature to a 1000 ^{o}C. However, upon closer scrutiny of the data, we have discovered that the phase at higher temperatures essentially increases linearly with temperature which is not the case at lower temperatures. Thus, a single polynomial

cannot fit the entire data. Therefore, now, we have broken the data up into three different ranges and fit three different polynomials, one for each range. The resulting TOC calculation is shown in Fig. 6.1.7. Here, the blue, red and black lines correspond to the three sets of data taken. As can be seen from this TOC calculation, at temperatures greater than about 550 ^{o}C, the TOC of SiC changes very little and essentially becomes constant at about 8 x 10^{-5} / ^{o}C.

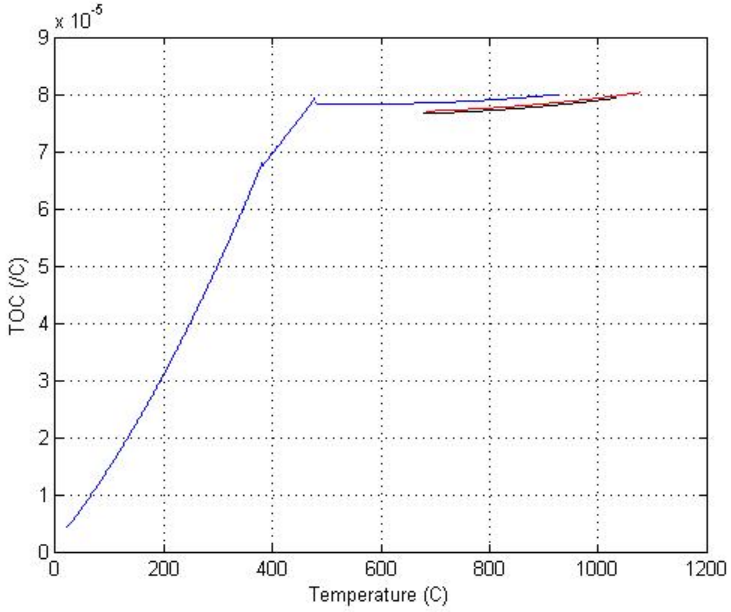

Fig. 6.1.7. Calculated Thermo-optic Coefficient (TOC) as a function of oven temperature

With respect to the Figure 5.1.2 the experimental setup, frames are captured at 1/30 s intervals just after the heating element at 90 ^{o}C is brought in contact with the chip. The fringes in the interferogram start moving in less than 1/30 th of a second while it takes almost 16 s for the SiC chip to reach the temperature of the heating element when the fringes are observed to stop moving. Next, the heating element is withdrawn from the chip using the PC actuator control and the fringes are again observed to move, but this time in the opposite direction. Again, the fringes start to move in less than 1/30 th of a second once the heating element is withdrawn and it takes almost 17 s for the chip to cool down to room temperature and for the fringes to stop moving. Note that in this case, heating of the SiC chip is a conductive process while the cooling is a radiative and convection-based process. The temperature of the SiC chip as a function of time is shown in Fig. 6.1.8 and shows similar heating and cool-down curves.

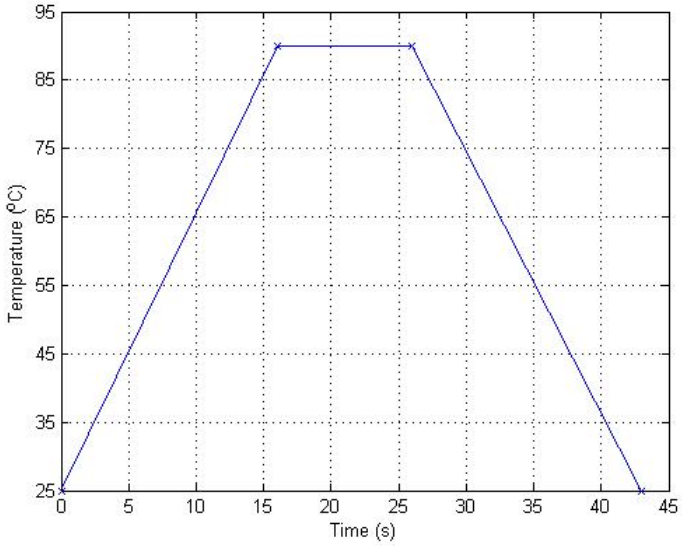

Fig. 6.1.8 The plot of SiC chip temperature vs time elapsed after placing the chip in contact with the heating element acting as a thermal step function which is at a stepped temperature of 90 ^{o}C.

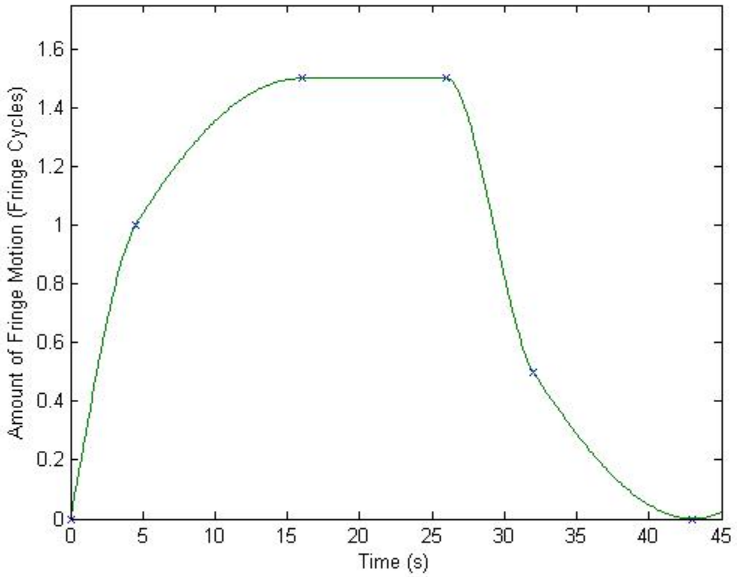

Fig. 6.1.9 Plot depicting the fringe movement with time elapsed after the SiC chip was placed in contact with the heating element acting as a thermal step function.

Fig. 6.1.9 shows the movement of the fringes from the time the heating element touches the chip till the time the heating element is removed and the steady state under room conditions is reached. When the heating element is placed in contact with the chip, the fringes start to move and the fringe pattern moves by ~ 1.5 fringes till a steady transient state is reached. No fringe movement is seen once this steady state has been reached. Then the heating element is removed from contact with the chip. The chip starts to cool under the influence of the room temperature and the fringe movement is the opposite

direction is observed again by ~1.5 fringes such that the original fringe pattern is seen when the steady state after cooling is observed.

With respect to the Figure 5.1.3 the experimental setup shown in Fig. 6.1.10 as the distributed sensor network system set-up in the laboratory. For fiber-optic network design principle demonstration, a 1x2 or N=2 MEMS switch design is implemented using one 1x2 MEMS fiber-optic switches. One chosen output fiber from the N=2 fibers is connected to the all-SiC frontend probe. The physical interconnection comprising the steel jacketed SMF connecting the 1xN switch output port to the all-SiC probe entry point is 15 m. This fiber is connected to a fiber lens whose minimum beam waist sits at a 60 cm distance from the fiber lens; in other words, the fiber lens half-self imaging distance is 60 cm for high efficiency SMF light coupling.

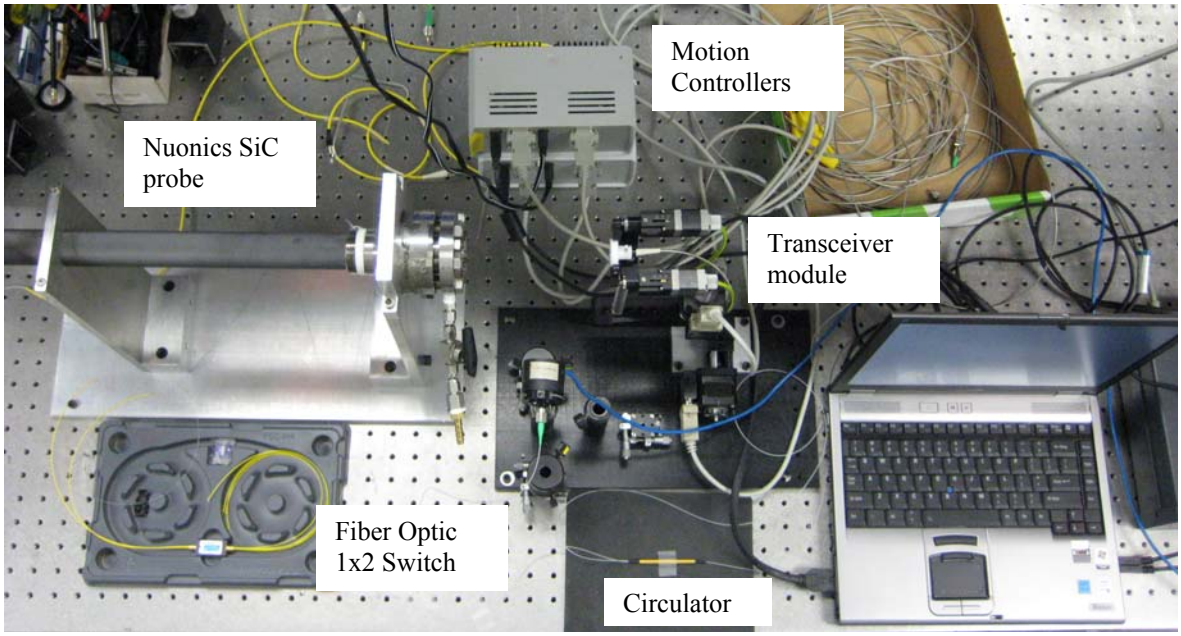

Fig. 6.1.10 The assembled fiber-optic sensor network demonstration using the all-SiC frontend probe and light misalignment tests.

The fiber lens is held in a mechanical assembly with piezoelectrically controlled tip/tilt and translational motion controls. Hence electrical control wires from a controller box feed the fiber lens mechanics. The controller boxes are connected to a lap-top computer that runs the motion controller software. The light exiting the fiber lens passes through a Magnesium Floride (MgF_2) optical window that seals the all-SiC probe from external air turbulence effects. The window is designed as a weak wedge, thus eliminating undesired window back-reflection interference effects that will effect sensor performance. The sensor probe is placed in a mechanical casing that simulates the combustor insertion point and chamber. Light from the remotely located tunable laser passes through a fiber-optic circulator to pass through the MEMS switches to enter the 15 m remoting fiber to the probe. The probe is aligned so that laser light from the tunable laser hits the embedded SiC chip at normal incidence and is reflected back into the fiber lens. Approximately

32% of the light at maximum (positive) interference is retro-reflected from the SiC chip which translates into a loss of 4.96 dB. The returning light via the steel jacketed 15 m SMF passes through the switches, circulator, to enter the power meter. Various two way optical losses in the sensor network system are due to MgF_2 optical window (0.89 dB), circulator (3.27 dB), 1x2 switch (1 dB), Free-space to Fiber Lens (FL) coupling loss (0.7 dB), and fiber connectors (0.3 dB). Thus total optical loss in the system amounts to 11.12 dB. The input power from the tunable laser to the system is 8.70 dBm while the detected output power is -2.55 dBm which is consistent with the loss numbers. The measured optical power data also indicates that the light indeed hits the SiC chip at normal incidence to enable full retroreflective self-imaging high efficiency coupling into the SMF.

To implement robustness tests, the system is deliberately misaligned so that the output optical power drops from a peak value of 0.222 mW to 0.080 mW. As shown in Fig. 6.1.11, using the computer-controlled motion stages, the peak optical value is entirely recovered.

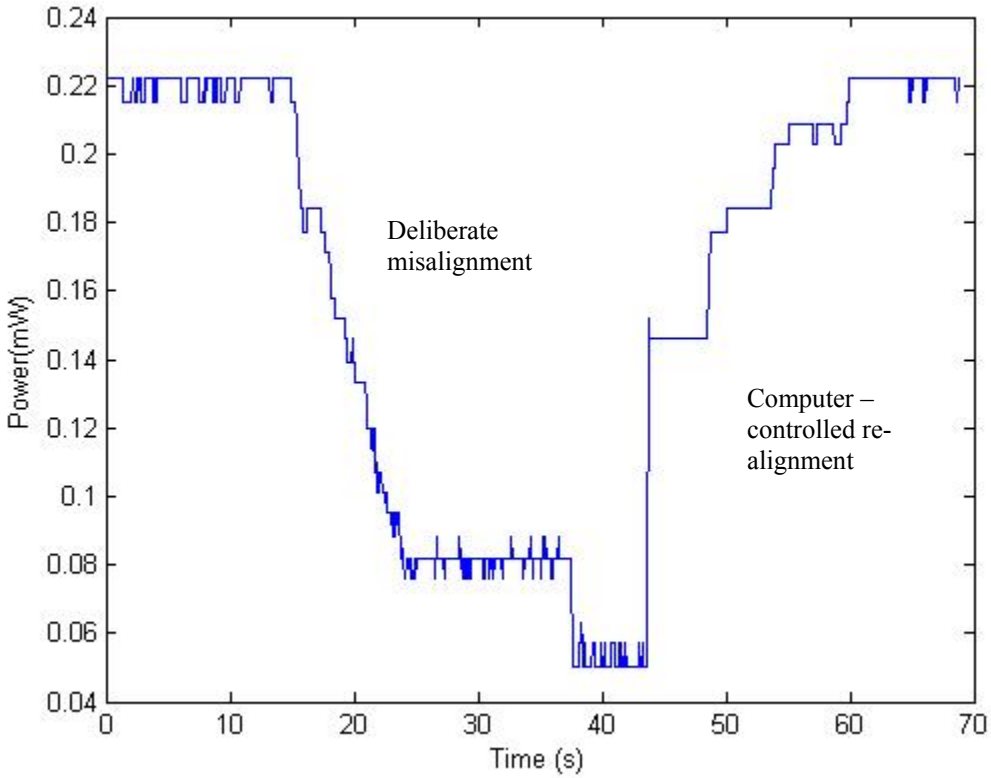

Fig. 6.1.11. Time trace of reflected power off the SiC chip when the all-SiC probe is deliberately misaligned and then re-aligned using computer-controlled motion stages on the fiber lens.

Specifically, Fig. 6.1.11 shows a time trace of the output power during the complete alignment procedure. The fiber-lens transceiver module has four degrees of electronic motion control. These four directions are the tip, tilt, x-translation, and z-translation. When the SiC chip reflected beam gets misaligned, the controls for each of these four

directions are adjusted individually one after the other such that the received optical power is maximized. Since the received optical power is not individually dependent on the position of the four controls but is in fact a joint function of the location of all the four controls, more than one adjustment iteration is required to optimally maximize the received power. A computer based alignment algorithm can efficiently execute the proposed alignment operations.

With respect to the Figure 5.1.4, test rig optical sensor data is analyzed to study sensor temporal and temperature responses.

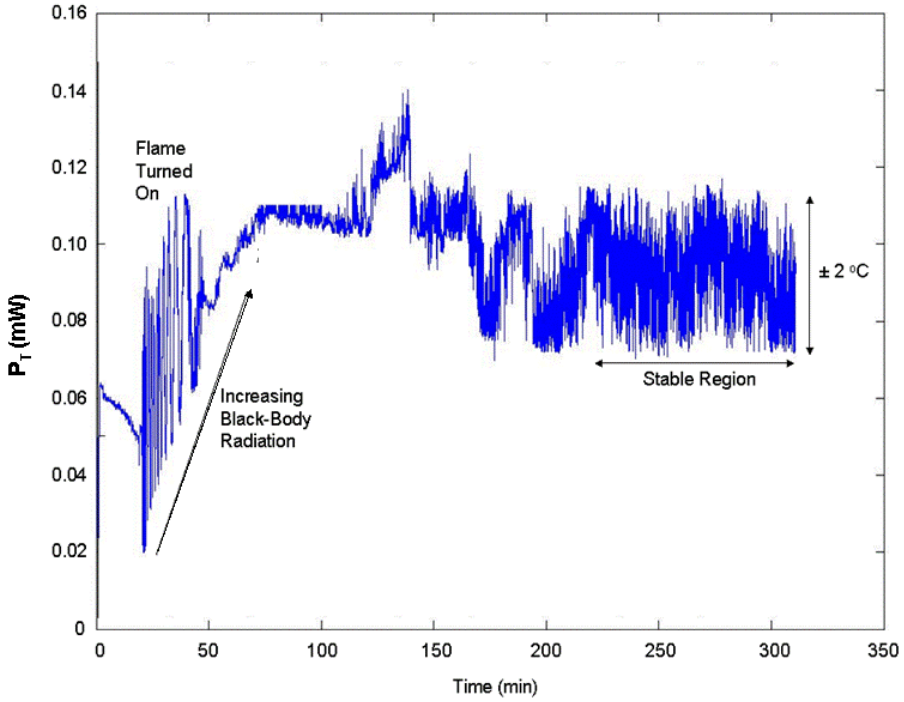

Fig. 6.1.12. Raw optical data recorded by the probe PD indicating the rig thermal ramp zone and the relative high temperature stabilization zone. Vertical axis is measured optical power in mW; Horizontal axis is a time counter.

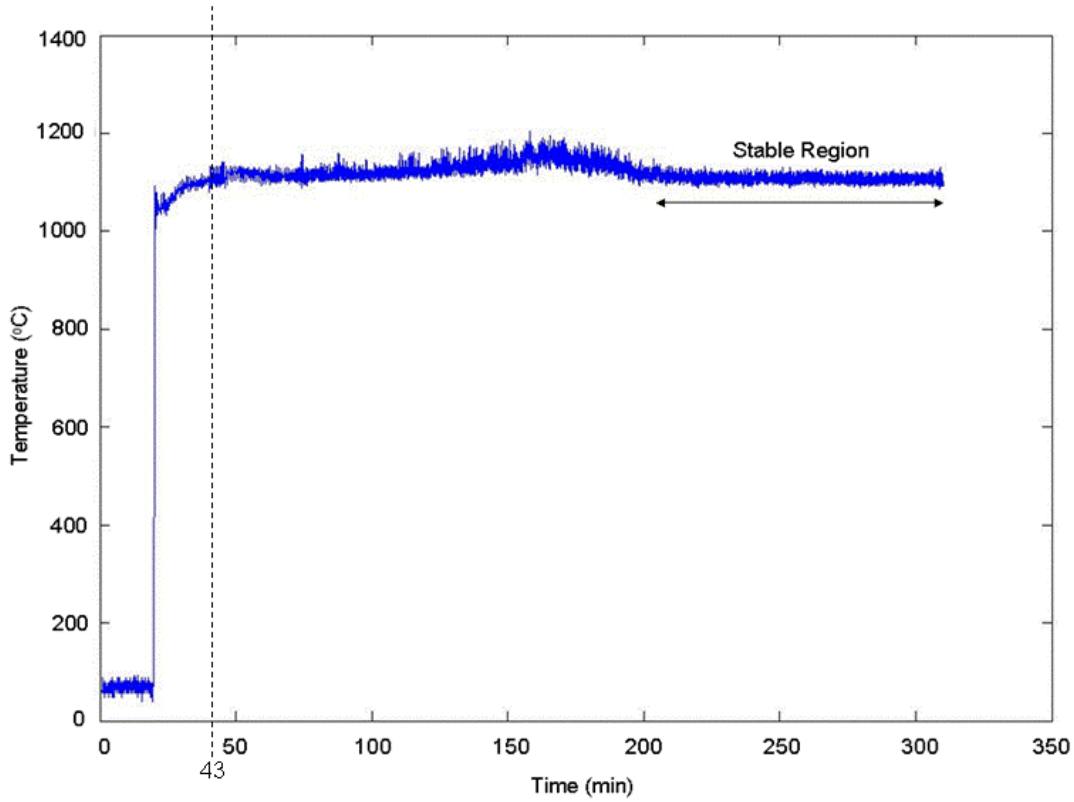

Fig. 6.1.13 Rig TC provided temperature reading during the Fig.2 optical data acquisition period. This TC data is used for optical probe calibration. Vertical axis is measured temperature; Horizontal axis is a time counter. A 43 min marker line indicates when the rig gas temperature near TC settles down in its high temperature range that is 23 min after thermal shock.

Fig. 6.1.12 shows the raw optical data provided by the all-SiC sensor PD. For the same test, Fig. 6.1.13 shows the equivalent temperature readings provided by a TC in the rig. After the flame light-up, the rig gas temperature near the TC after a ~ 23 min time interval (see TC data) settles into its expected high temperature operational range with measured TC maximum temperatures reaching 1239 ºC. One can clearly see the expected Fabry-Perot effect oscillatory behavior of the optical power during thermal ramping. In addition, the optical power picks up an increasing bias level due to increasing BB radiation during ramping. In addition, the optical power continues to oscillate depending on the rig temperature fluctuations at the set higher temperature zone. This is so as the optical sensor is designed to be sensitive to high temperature zone changes in a 20 ºC increment indicating that optical power goes from a peak to a null if temperature changes by 10 ºC. This feature points to the fact that the optical sensor can measure temperature to a very high accuracy given the optical power meter is highly sensitive.

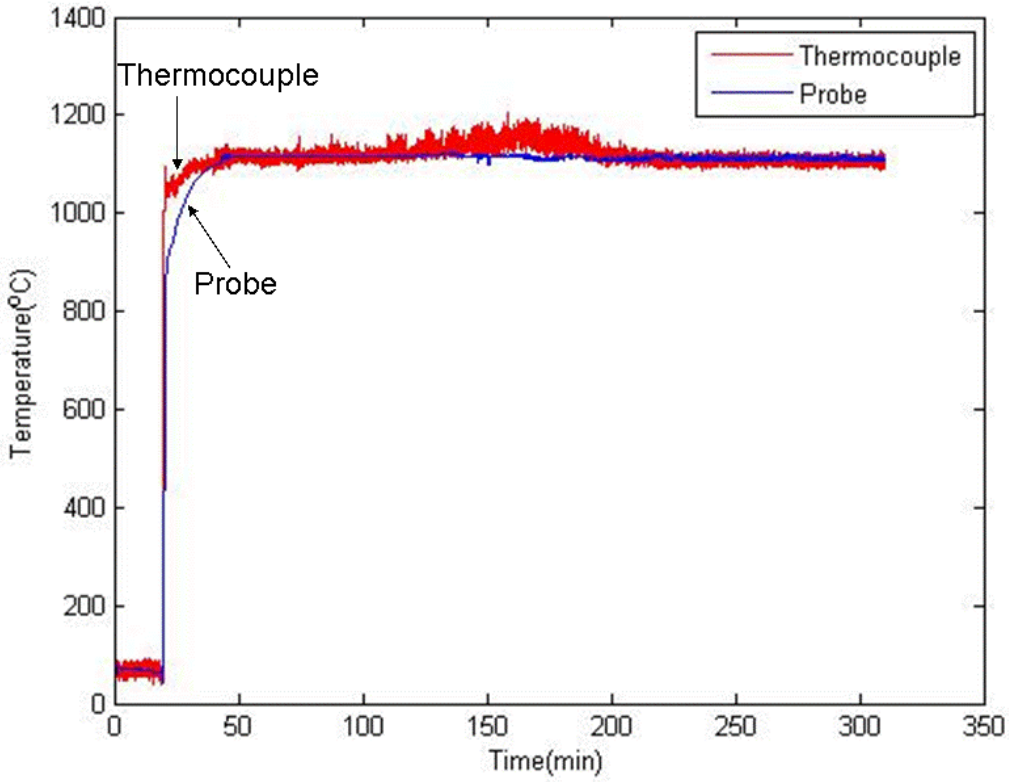

Fig. 6.1.14 Comparative optical probe and TC measured temperatures over the duration of the rig operation.

Do note that in the thermal shock region, the all-SiC optical probe did respond in real-time (or video rate) indicated by the rapidly pulsating on/off laser beam images with a 33 ms video time interval. The Fig. 6.1.14 curve shows that the stable region average temperature of the gas in the rig is 1107 ºC and the SD in the indicated 60 minutes stable region is ± 6.3 ºC and ± 2 ºC given by the TC and SiC probe, respectively. Using the Fig. 6.1.12 BB radiation data (provided by the DC bias level of the recorded optical power) and its equivalent temperature values from the TC data, Fig. 6.1.14 shows the measured optical probe temperatures over the whole duration of the rig operation. Using Fig. 6.1.14 data, a thermal time constant of 10 s is computed for the TC as this is the time it takes for the TC to reach 63.2% (or 1-1/e) of the difference between the thermal ramp start and end temperatures or for T=0.632·(1050-87)+87 = 695 °C. In comparison, the thermal time constant for the all-SiC probe is computed as a TC comparable 18 s. This dynamic temperature measurement response of the SiC probe owes its behavior to the probe's large thermal mass via its present physical size and its current non-optimal thermal refractory insulation experimental conditions. This environment and packaging for the SiC probe can be greatly improved to deliver even better temporal responses.

6.2 Part 2 of Program

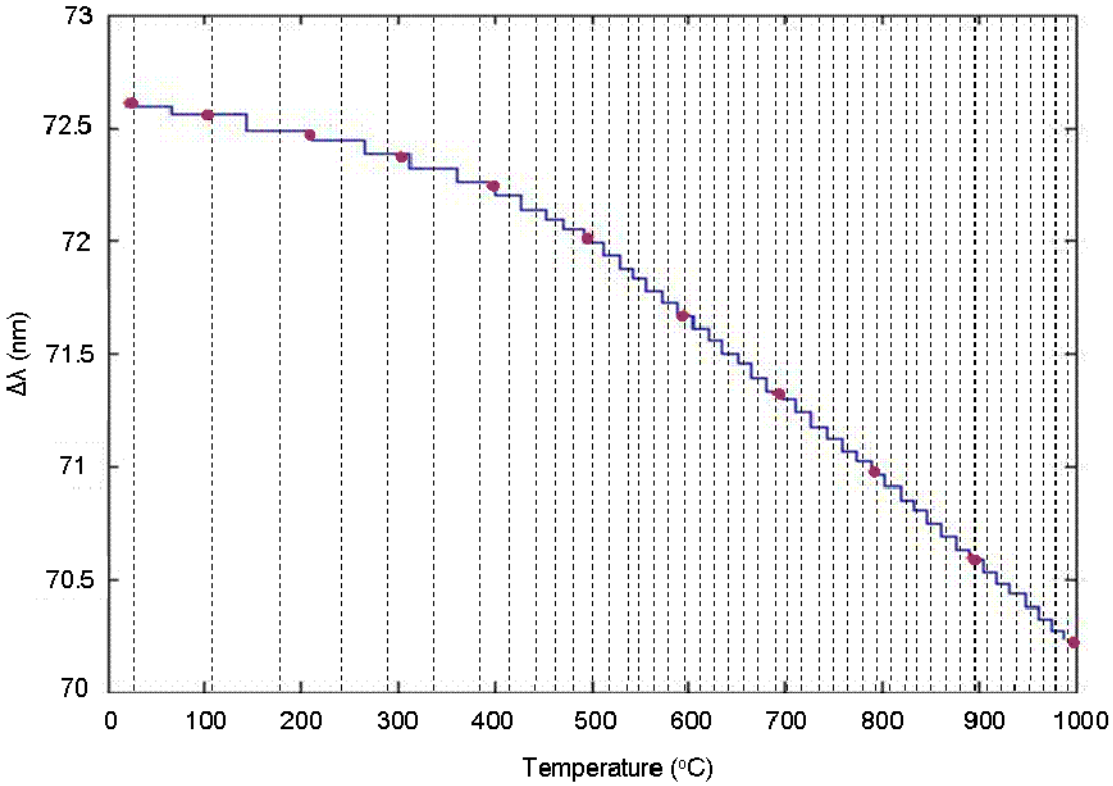

Fig.6.2.1 Experimentally measured coarse temperature sensing Δλ vs. T step-wise curve with k = 60.

The Fig.5.2.1 proof-of-concept sensor is set up in the laboratory with the all-SiC probe placed in a high temperature oven. The tunable laser source (TL) used is a Santec Model TSL-210 with a peak power of 10 mW, a wavelength tuning range of 1520-1600 nm and tuning resolution of 0.01 nm. The Fiber Lens (FL) has a half self-imaging distance of 60 cm and a $1/e^2$ minimum beam waist of 0.53 mm formed at the SiC chip at the end of the fabricated probe.

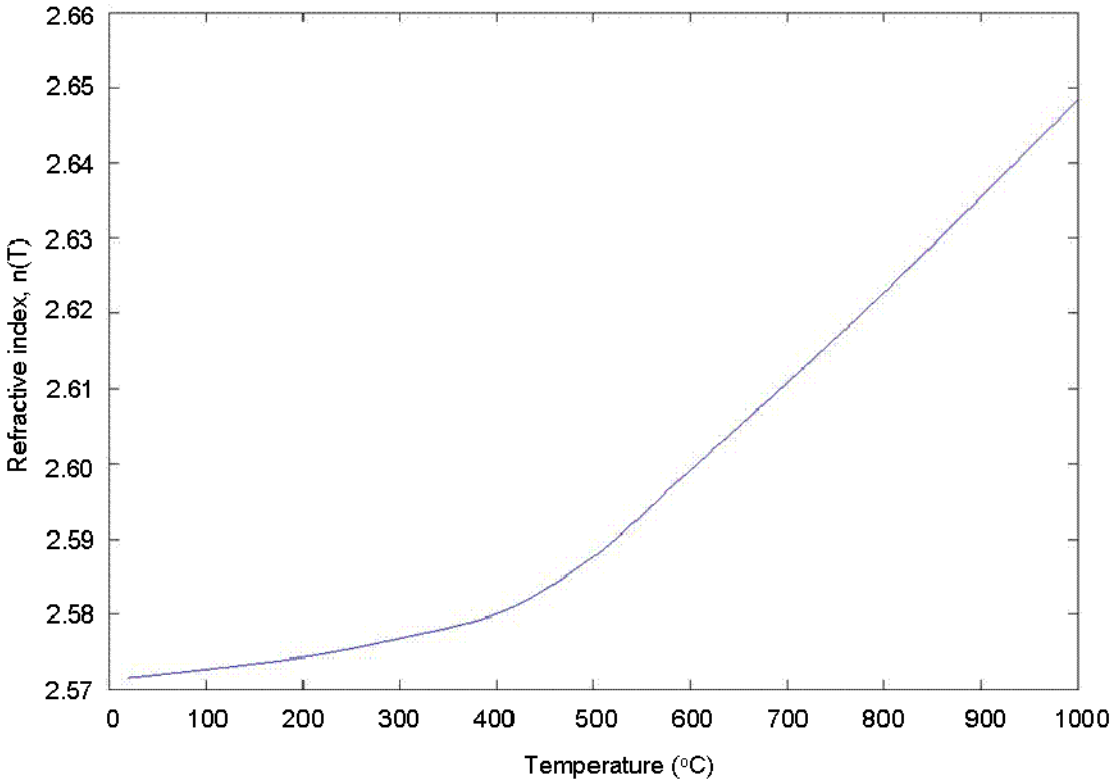

Fig. 6.2.2. Computed SiC refractive index n versus temperature T curve using Section. 5.2 Eq. 2 and Fig.6.2.1 data.

The SiC chip has a thickness t = 389 μm at room temperature. The probe is placed in the oven through a hole in the oven. Light from FL passes through an optical Window (W) and the fabricated probe cavity to strike the SiC chip at normal incidence. In the return path, the reflected light is deflected using a Beam Splitter (BS) and is focused onto a 3 mm diameter Newport Photo-Detector (PD) using a 10 cm focal length spherical lens S. The reference oven temperature is measured via an R-type TC. The oven temperature is set at approximately 100 ^{o}C intervals from 22 ^{o}C room temperature to 1000 ^{o}C. Optical readings are taken for $\Delta\lambda$ with k = 60 and λ_{peak} within one FSR around λ_c = 1550 nm (at m = 1286 for T = 22 ^{o}C). The experimental $\Delta\lambda$ vs. temperature data (see Fig. 6.2.1) shows that the value of $\Delta\lambda$ varies step-wise from 72.62 nm to 70.22 nm as the temperature goes from 22 ^{o}C to 1000 ^{o}C. Using this curve and section 5.2 Eq.2, SiC refractive index n_1 at wavelength λ_1 = 1550 nm is determined as a function of temperature (see Fig. 6.2.2). Next, using Eq.5 and Fig.6.2.1 data, expected theoretical values of λ_{peak} within one FSR around λ_c = 1550 nm as a function of temperature are calculated.

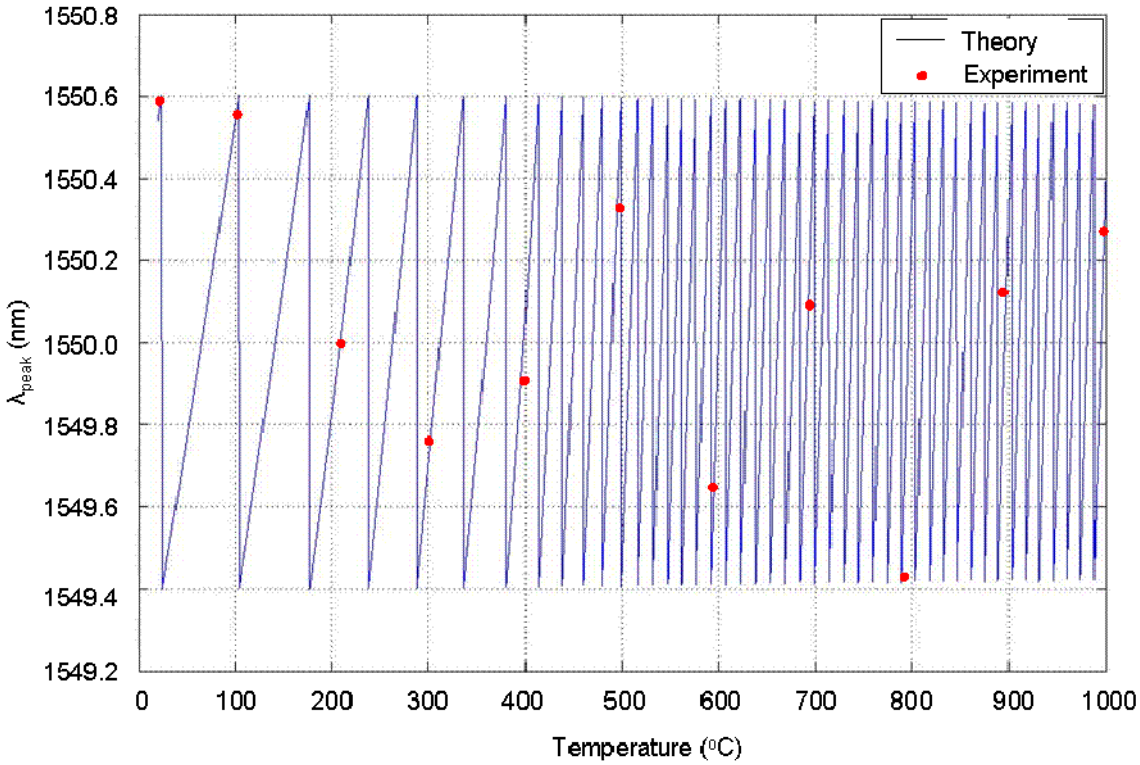

Fig. 6.2.3 Computed and experimentally measured (11 data points) λ_{peak} versus temperature curve for fine temperature sensing.

This λ_{peak} vs. T curve shown in Fig.6.2.3 has a saw-tooth like behavior since only the location of the peak within one FSR is plotted. The temperature change required for λ_{peak} to go from one end of the FSR to the other is not uniform over the whole range as the change in refractive index of SiC with temperature is non-linear. Hence, the temperature sensing resolution is higher for higher temperatures, a feature suitable for the extreme temperature gas turbine application. Fig. 6.2.3 also shows some sample experimentally measured λ_{peak} values showing close agreement between theory and experiment.

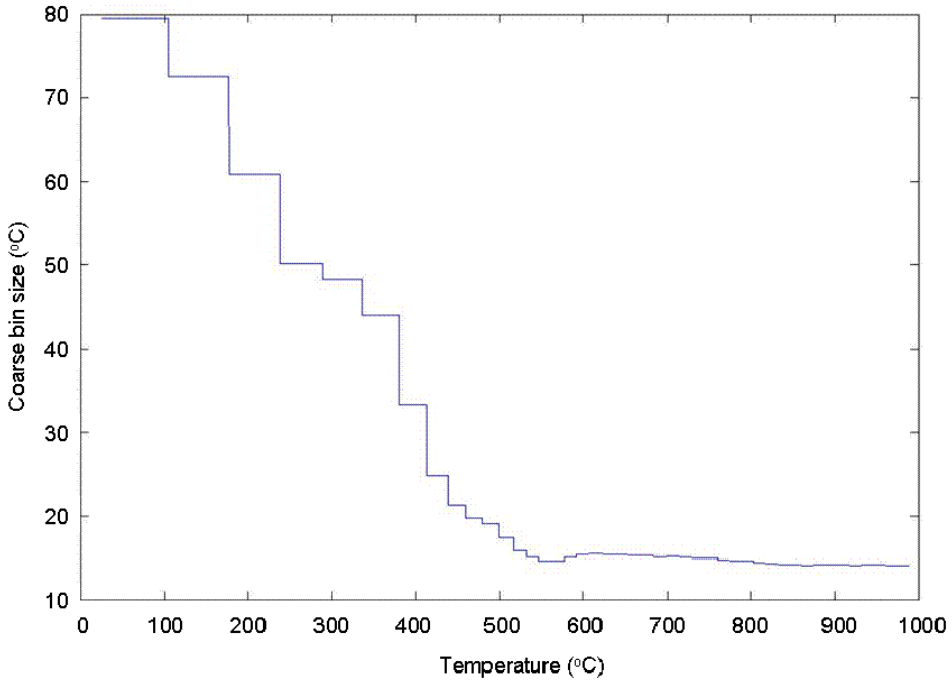

Fig. 6.2.4. Computed coarse measurement bin size versus temperature.

The whole temperature range can be divided into many specific coarse bins. Within each coarse bin, the temperature can be uniquely determined by tracking the location of the peak wavelength. These coarse bins can be computed from Fig.6.2.3 data and are shown as a function of temperature in Fig.6.2.4. The coarse bin size varies from 79 ^{o}C at room temperature to 14 ^{o}C at 1000 ^{o}C. These coarse bins are also shown marked on Fig. 6.2.1 as vertical dashed lines indicating how a specific measured value of $\Delta\lambda$ can be used to determine in which coarse bin the temperature being measured belongs. The change in $\Delta\lambda$ from one coarse bin to the next for k = 60 is found to vary between 0.04 nm and 0.05 nm, well within the 0.01 nm tuning resolution of the laser.

Table 1. Measured temperature using the proposed temperature sensor and R-type thermocouple.

TC MEASURED TEMPERATURE (^{O}C)	OPTICAL SENSOR MEASURED TEMPERATURE (^{O}C)	PERCENTAGE DIFFERENCE
21.8	22.9	5.0
102.0	100.8	1.2
209.0	209.1	0.048
303.0	302.3	0.23
397.6	395.7	0.48
496.2	494.6	0.32
595.7	594.9	0.13
693.3	692.8	0.072
791.5	789.3	0.28
894.0	897.6	0.40
997.2	998.4	0.12

The temperature resolution of the sensor can be determined by dividing the coarse bin size by the number of fine temperature bins N_f inside each coarse bin, i.e., N_f = FSR / (Laser Tuning Resolution). Since the ~1.2 nm FSR changes by a small amount (< 0.04 nm) over the whole temperature range, N_f is ~1.2 nm / 0.01 nm = 120 bins. With the coarse bin size getting smaller at higher temperatures, one improves the resolution of the sensor. The calculated resolution of the demonstrated sensor varies from 0.66 ^{o}C at room temperature to 0.12 ^{o}C at 1000 ^{o}C. Table 1 shows the measured sensor temperature readings using the Fig. 6.2.1 and Fig. 6.2.3 eleven data points and compares them with the oven TC readings. The results indicate temperature percentage differences of less than 1% for temperatures greater than or equal to 200 ^{o}C. Note that the oven TC had a specified measurement resolution of ± 0.1% of the temperature reading giving a ±1 ^{o}C resolution for a 1000 ^{o}C temperature. Unlike precious metal TCs, the proposed sensor does not fundamentally limit its resolution as a percentage of the measured temperature, for example, giving a much improved 0.12 ^{o}C resolution at 1000 ^{o}C.

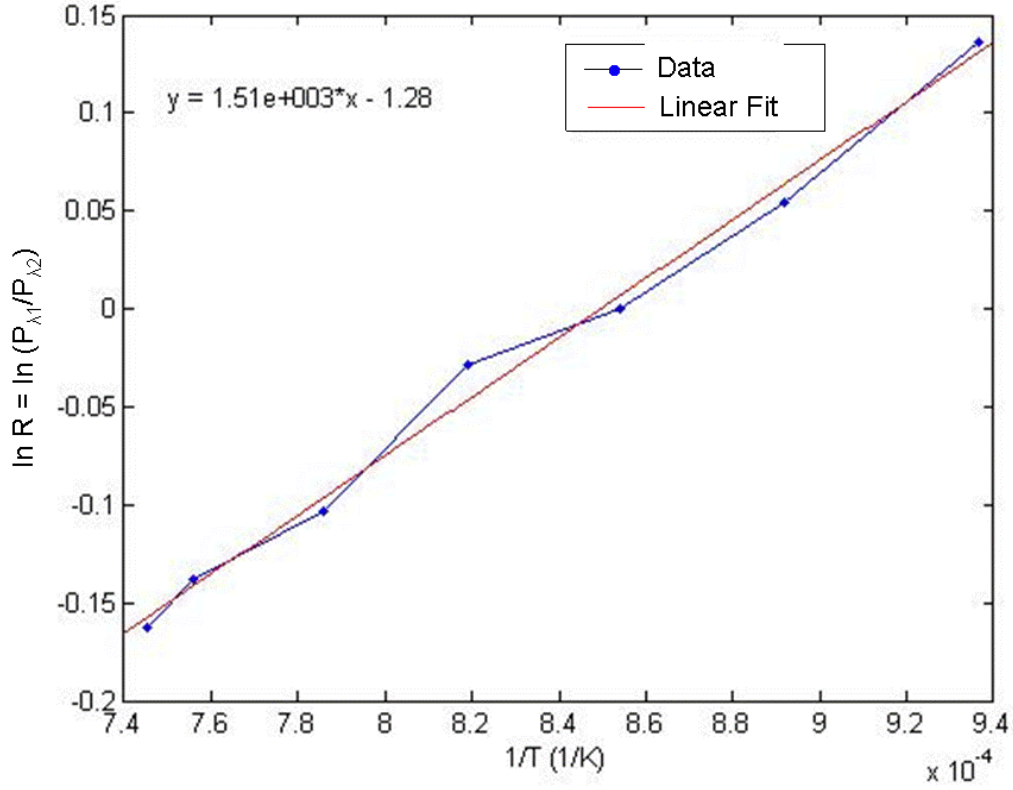

Fig. 6.2.5. Experimentally measured ln R vs. 1/T curve and the corresponding line of best fit.

The Fig. 5.2.2 proof-of-concept experiment is set-up in the laboratory with SiC chip t = 389 μm. The probe is inserted into an oven. BB radiation from the SiC chip and the background passes through an optical window W. After deflection from the beam-splitter BS1, radiation is captured using a 10 cm focal length spherical lens S and directed towards another beam splitter BS2 and then towards two 3 mm diameter Newport photo-detectors PD1 and PD2. Optical filters F1 and F2 are Newport laser line models 10LF30-1550 and 10LF30-1300 having center wavelengths λ_1 and λ_2 of 1550±7 nm and 1300±7

nm, respectively. The filters have a FWHM bandwidth of 30±7 nm. An R-type TC is used to measure the oven reference T. For laser interferometry is used a tunable laser TL Santec TSL-210 with a wavelength tuning range of 1520-1600 nm and peak power of 10 mW. The Fiber Lens FL has a working distance of 60 cm and $1/e^2$ minimum beam waist diameter of 0.53 mm formed at the SiC chip. Light from the FL strikes the SiC chip at normal incidence and in the return path, is deflected from BS1 and BS2 and is focused onto PD1. TL is set to $\lambda_L = 1550$ nm.

The oven is set at ~ 50 ^oC intervals starting at T = 795 ^oC. Optical power meter PM readings are taken with TL on and with TL off. Fig. 6.2.5 shows how ln R varies with 1/T and a linear line of best fit is found in accordance with Eq.8 that in-turn gives $\alpha = -1.282$ and $\beta = 1509$. Note that if the Wein approximation is not used and instead the exact Planck's BB radiation formula is used, $\alpha = -1.285$ and $\beta = 1512$. Given that the proposed sensor uses pyrometry for coarse temperature measurement, using the Wein approximation is justified and leads to simpler signal processing. Assuming that the center wavelengths of the laser line filters are 1543 nm and 1307 nm within the manufacturer tolerance limits, the theoretical value of β from Eq. 7 and Eq. 8 is found to be 1684. Note that the linear model in Eq. 8 is developed under the assumption that $A_S(\lambda)$ $\varepsilon(\lambda,T)$ and $a(\lambda,T)$ in Eq. 7 are all independent of λ. In practice, these are all weakly dependent on λ and this can cause deviation of β from the theoretical value. Fig. 9 shows the R against T calibration curve extrapolated to 1600 ^oC based on the linear fit from Fig. 6.2.5. A coarse value of the temperature can simply be found by measuring R and finding the corresponding T value from Fig.6.2.6. Note that this calibration curve is only valid for the Fig.5.2.2 specific experimental arrangement, i.e., heating via the deployed oven with its specific background radiation in the output detected power. For a different heating environment, the sensor would have to be re-calibrated to take into account the differing levels of background radiation. Note that for the sensor to be used in all environments, sensor calibration requires the background radiation to be blocked at the λ_1 and λ_2 wavelengths of interest. This can readily be achieved by using a capped frontend all-SiC probe design that would prevent optical background radiation from entering the light paths to the detectors. Such a design would also prevent the SiC chip from coming into direct contact with contaminants such as water vapor present in the extreme turbine environments, thus preventing elevated temperature oxidation of the SiC sensor chip. In addition, the all-SiC probe cavity is closed using the optical window W and a partial vacuum (25in Hg) is maintained inside the probe. Ideally, a vacuum or hermetic sealed probe would remove any possibility of the SiC chip and SiC probe internal cavity from oxidizing.

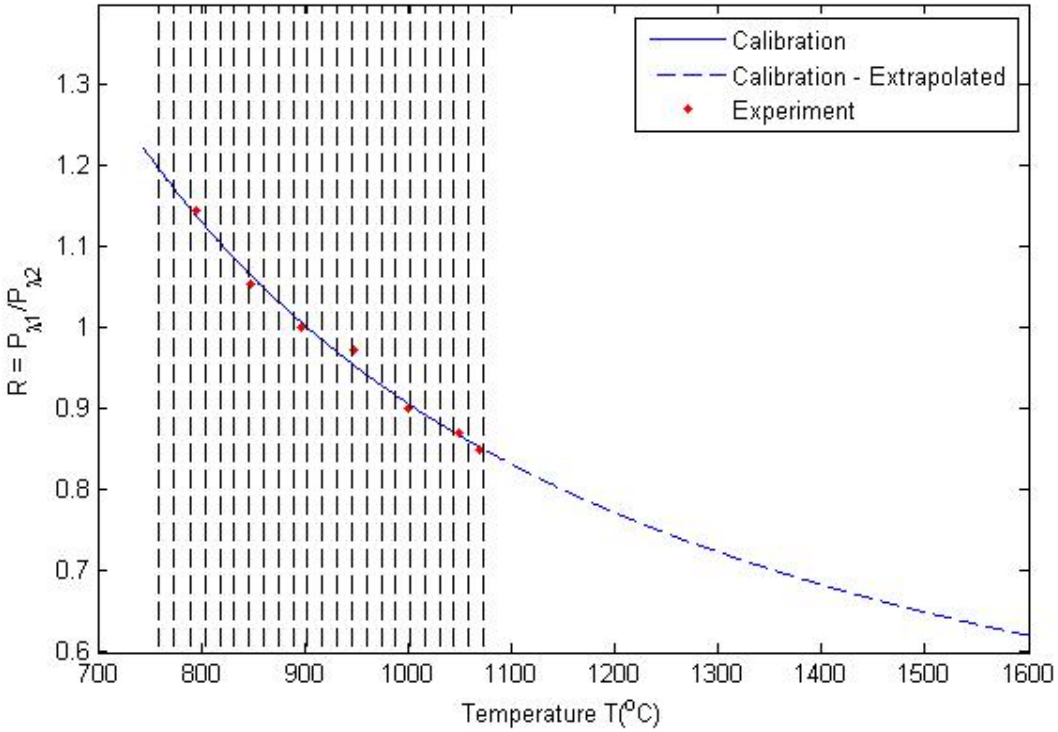

Fig.6.2.6. R vs. T calibration curve using α and β derived from curve fitting along with experimentally measured temperatures using optical pyrometry.

The resolution of the pyrometer depends on the smallest change in optical power that can be detected by PD1 and PD2 (with laser off) based on the noise present in the system. The change in T due to a change in R can be written by differentiating Eq. 8 with respect to R and is given as:

$$\Delta T = \frac{-\beta}{R(\ln R - \alpha)^2}\Delta R . \qquad (12)$$

Using Eq. 7 and taking partial derivatives of R with respect to $P_{\lambda 1}$ and $P_{\lambda 2}$, ΔR can be further written in terms of change in detected powers $P_{\lambda 1}$ and $P_{\lambda 2}$ as:

$$\Delta R = \frac{\Delta P_{\lambda_1} - R \cdot \Delta P_{\lambda_2}}{P_{\lambda_2}} . \qquad (13)$$

The smallest change in radiation power that can be detected based on the noise in the present system is $\Delta P_{\lambda 1} = \Delta P_{\lambda 2} = 0.01$ μW. At T = 795 °C, R = 1.14 and $P_{\lambda 2} = 0.16$ μW while at T = 1077 °C, R = 0.85 and $P_{\lambda 2} = 0.80$ μW. Based on these numbers and using Eq.12 and Eq. 13, the resolution of the pyrometer is estimated to vary between 5.8 °C at 795 °C to 2.7 °C at 1077 °C. Note that this resolution is sufficient to identify the correct 2π cycle for fine temperature sensing as each cycle is approximately 15 °C. Recall that FP laser interferometry (used for fine temperature sensing) can only be used to determine temperature unambiguously within one 2π cycle of the P_{norm} against φ curve. These 2π cycles are shown marked on Fig. 6.2.6 as vertical dashed lines indicating how a specific measured value of R can be used to determine in which 2π cycle the temperature being

measured belongs. The experimentally measured R values are also shown in Fig. 6.2.6 that are used to identify the 2π cycle to which the temperature belongs. Once the correct 2π cycle is identified, then with the TL on, the PD1 power is measured that includes both laser reflected power as well as the BB radiation power. The laser reflected power, however, is much greater than the radiation power and is normalized by simply tuning the wavelength to find localized power maxima and minima values and using Eq.11 to find P_{norm}.

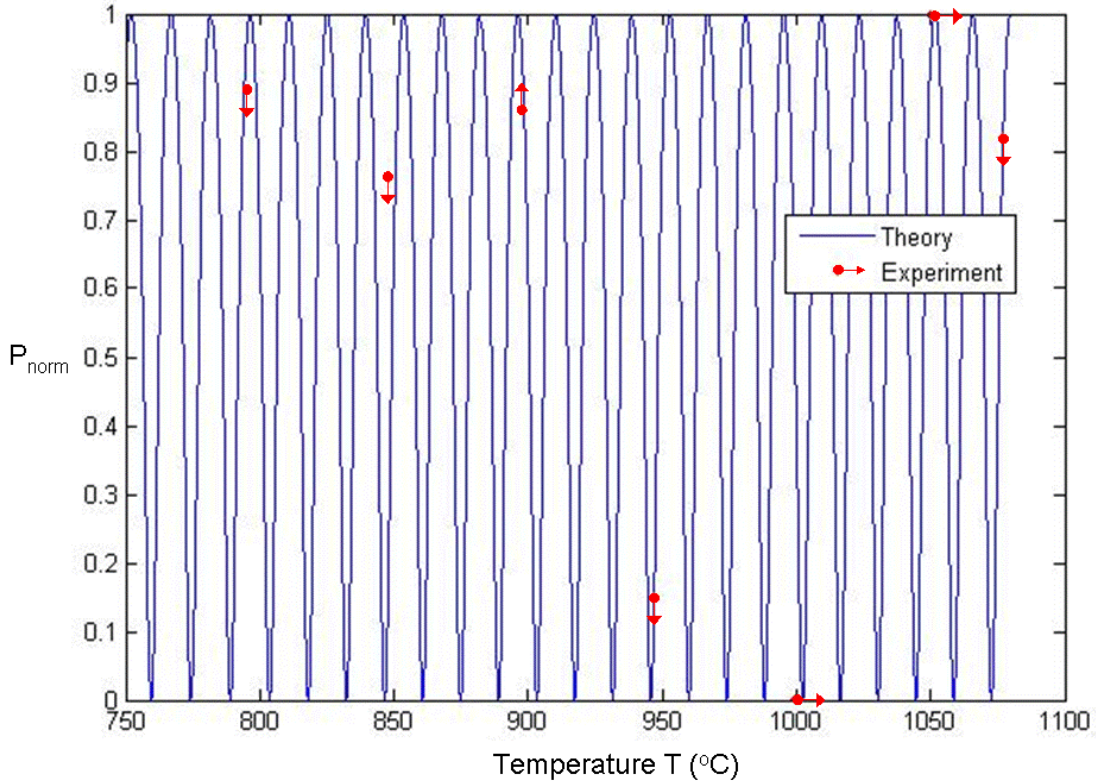

Fig. 6.2.7. Computed and experimentally measured P_{norm} against T curve for fine temperature sensing.

Also, by tuning the wavelength, the direction of the change in power with wavelength is determined (shown by arrows in Fig. 6.2.7) in accordance with Eq. 10 to distinguish between the two halves of the 2π cycle. These results are shown in Fig. 6.2.7 along with the expected theoretical curve for the normalized laser reflected power with temperature based on previous experiments. The T resolution for this laser technique (and sensor) is also determined by the smallest change in optical power detected by PD1 (with laser on) based on the noise in the system. This smallest change is measured to be $\Delta P = 0.001$ mW with a $P_{max} - P_{min} = 0.079$ mW for an average 7.5 ^{o}C change in T. These numbers give an estimated average 0.1 ^{o}C resolution for the sensor. Table 2 shows comparative measurements of T using the TC, two color optical pyrometry, and the proposed hybrid sensor. The results show a sensor measured maximum T difference of 0.44 % compared to the TC readings.

Note that using the proposed hybrid sensing approach, an error in temperature measurement could arise if the temperature being measured lies close to the boundary of

the calibrated coarse temperature bins defined by the 2π temperature cyclic data (e.g., Fig. 6.2.7) via single wavelength laser-based FP interferometry of the SiC chip. Thus a slight experimental error in the coarse temperature measurement could result in identification of the wrong 2π cycle or coarse temperature bin leading to a large error in the signal processing-based measured temperature. Another issue related to the proposed signal processing is the possibility of reduced fine temperature measurement sensitivity (or resolution) controlled by the slope of the P_{norm} vs. T curve or dP/dT (see Fig. 6.2.7) close to the maxima or minima of this cyclic curve. Specifically, the slope of the curve approaches zero close to these max/min temperature points resulting in decreased sensor temperature measurement resolution. Both these mentioned signal processing limitations can be circumvented by calibrating the optical probe at two slightly different laser wavelengths λ_1 and λ_2 instead of one specific wavelength such that there is a π/2 to π phase difference between the two calibration curves (see Fig. 6.2.8). This process would result in two sets of coarse bin boundaries, one each for λ_1 and λ_2, relatively displaced from each other so that no temperature value could simultaneously lie close to the coarse bin boundary for both λ_1 and λ_2.

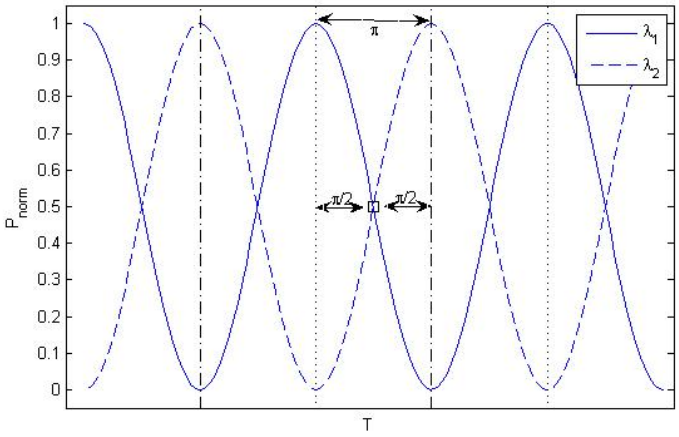

(a)

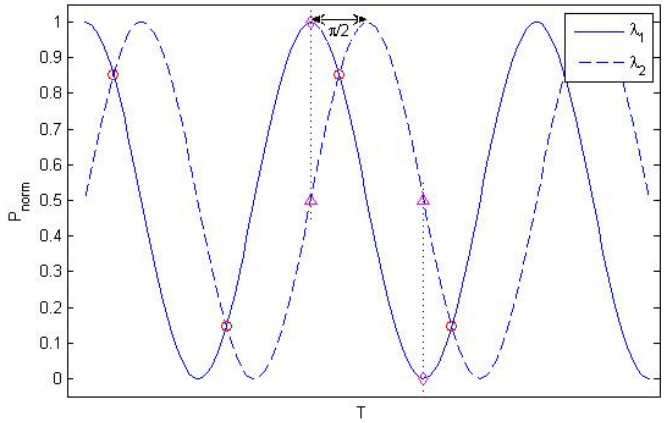

(b)

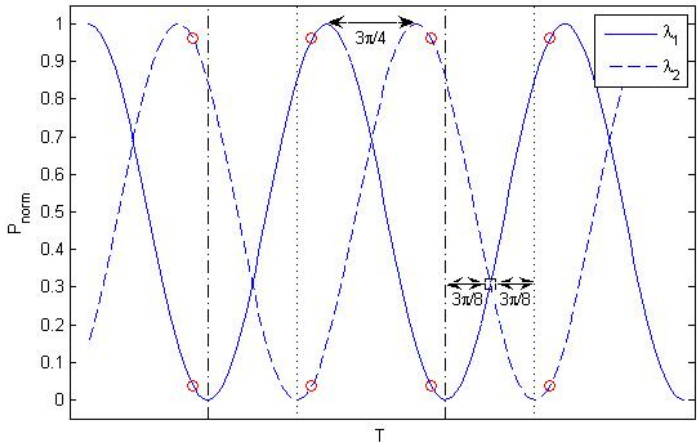

(c)

Fig. 6.2.8. Sensor signal processing calibration curves at two wavelengths λ_1 and λ_2 with relative curve phase differences of (a) π, (b) $\pi/2$, and (c) $3\pi/4$. Vertical lines in Fig. 6.2.8(a) and 6.2.8(c) denote the 2π cycle boundaries at each wavelength that determine sets of coarse bins for sensor calibration.

Note that if the coarse temperature measurement gives a temperature value that lies near the boundary for λ_1, then λ_2 could be used for fine temperature measurement to give an accurate temperature value and vice versa. At the same time, it would also ensure that any given temperature value would fall in the highly sensitive region of the P_{norm} vs. T calibration curve for at least one of λ_1 and λ_2 power readings, thus resulting in high resolution temperature measurement for all temperatures measured by the sensor. Note that for the coarse temperature boundary indecision problem, the ideal phase difference between the two calibration curves is π radians (see Fig. 6.2.8(a)) as it gives the highest discrimination between the two sets of laser power cycle boundaries. In the worst-case scenario shown by a square marker in Fig. 6.2.8(a), the measured temperature is at least $\pi/2$ radians away from a cycle boundary that for the present experiment would amount to ~4 °C (see Fig. 6.2.7 as 1 cycle is ~16 °C). Note that for optimal sensor temperature sensitivity, the ideal value for the calibration cyclic power two wavelength phase difference is $\pi/2$. This is because if the temperature value falls on the maxima or minima for λ_1, it also falls on the most sensitive part of the curve for λ_2 (see Fig. 6.2.8(b)) and vice versa. Example of these temperatures with the curve slopes of zero are indicated by diamonds on the P_{norm} vs. T curves in Fig. 6.2.8(b) and indeed show that their corresponding second wavelength power values (shown as triangles) fall on the highly sensitive parts of their second wavelength curve. The temperatures with the least sensitivity in this two-wavelength calibration scenario, $(\pi-\pi/2)/2 = \pi/4$ radians away from the maximas or minimas of both curves, are indicated by circles on the P_{norm} vs. T curve in Fig. 6.2.8(b) and still fall on highly sensitive parts of the curve. For the present experiment, this least sensitivity sensor temperature resolution would be 0.09 °C as found by numerically by finding the slope of the curve in Fig. 6.2.7 with a 0.001 mw optical power change. As shown in Fig. 6.2.8(c), calibration curves with relative phase shift value between π and $\pi/2$ would equally account for both coarse bin boundary and sensor resolution issues, although the specific choice of phase difference would depend on

experimental considerations such as the probability of error and the resolution of the coarse measurement. For example, using a phase difference of $3\pi/4$ (see Fig. 6.2.8(c)), any measured temperature is at least $3\pi/8$ radians away from a coarse bin boundary (shown as a square on the figure), or equivalently ~3 °C for the reported experiment. In this case, the temperatures with the least sensitivity (again shown by circles on Fig. 6.2.8(c)) are $(\pi-3\pi/4)/2 = \pi/8$ radians away from the maximas or minimas of both curves. Although the sensitivity is reduced from the case of Fig. 6.2.8(b), it is still comparable to the average value for the sensor. Specifically, for the present experiment this least sensitivity temperature resolution value is found from Fig.6.2.7 to be 0.16 °C.

TC T (^{O}C)	PYROMETER ONLY T (^{O}C)	SENSOR MEASURED T (^{O}C)
795.0	791.0	798.5
848.0	856.0	850.5
897.7	904.0	898.5
946.5	930.5	944.0
999.5	1006.5	1002.5
1049.0	1045.5	1051.5
1077.0	1069.0	1077.0

Table 2. Comparative measurements of T using TC, two color optical pyrometry, and the hybrid sensor.

6.3 Part 3 of Program

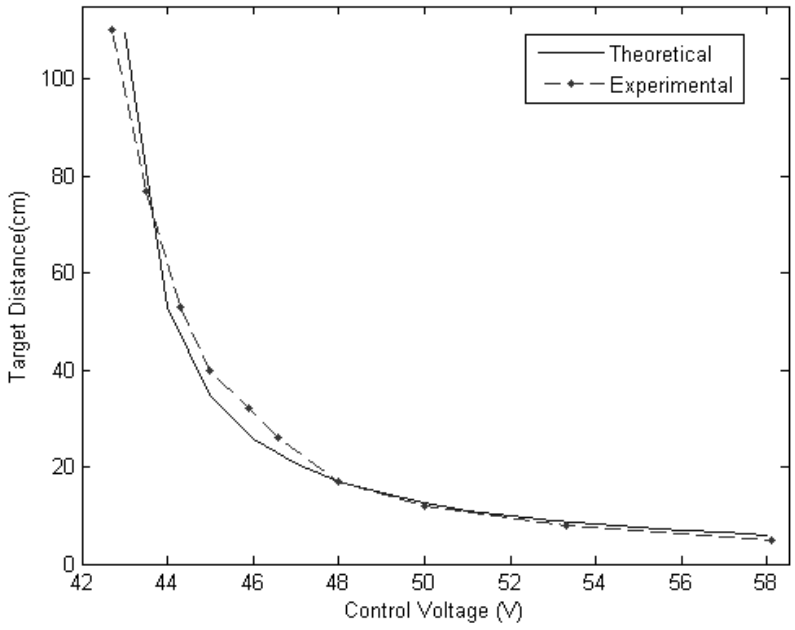

Fig.6.3.1 Sensor theoretical and experimental plots for the target distance versus the required ECVFL control voltage for formation of target minimum beam spot.

For a proof-of-concept experiment, the Fig.5.3.1 distance sensor has been set-up using the following experimental conditions: LS: 633 nm He-Ne laser; $\theta = 1.24$ mrad (0.0710 degrees); H = 0.3275 mm; 50:50 Glass BS, Target: Visible Mirror on Translation stage; ECVFL: Varioptic (France) Model Artic 320 Liquid Lens with voltage control step of $\Delta V_c = 200$ mV ranging from $V_c = 43$ V ($F_{max} = 21.28$ cm) to $V_c = 58$ V ($F_{min} = 4.89$ cm); ECVFL optical transmission efficiency at 633 nm is 92% and the reset time is 100 ms; $F_s = 10$ cm, $L_1 = 9$ cm. Given these conditions, one computes $D_s = 26.43$ cm, $L_2+L_3 = L_1 = 9$ cm, $F_v = D_s - L_1 = 17.43$ cm, $L_4 = 7.22$ cm, $D_{T\text{-}max} = 109.21$ cm, and $D_{T\text{-}min} = 6$ cm. Note that to preserve layout symmetry, $L_2=L_3= 4.5$ cm. The lens S is positioned to meet the computed $L_4 = 7.22$ cm distance that indeed is confirmed as the minimum spot distance when simultaneously observing the minimum spot formed on the target. Fig.6.3.1 shows the experimental results of the sensor which also matches the design theory.

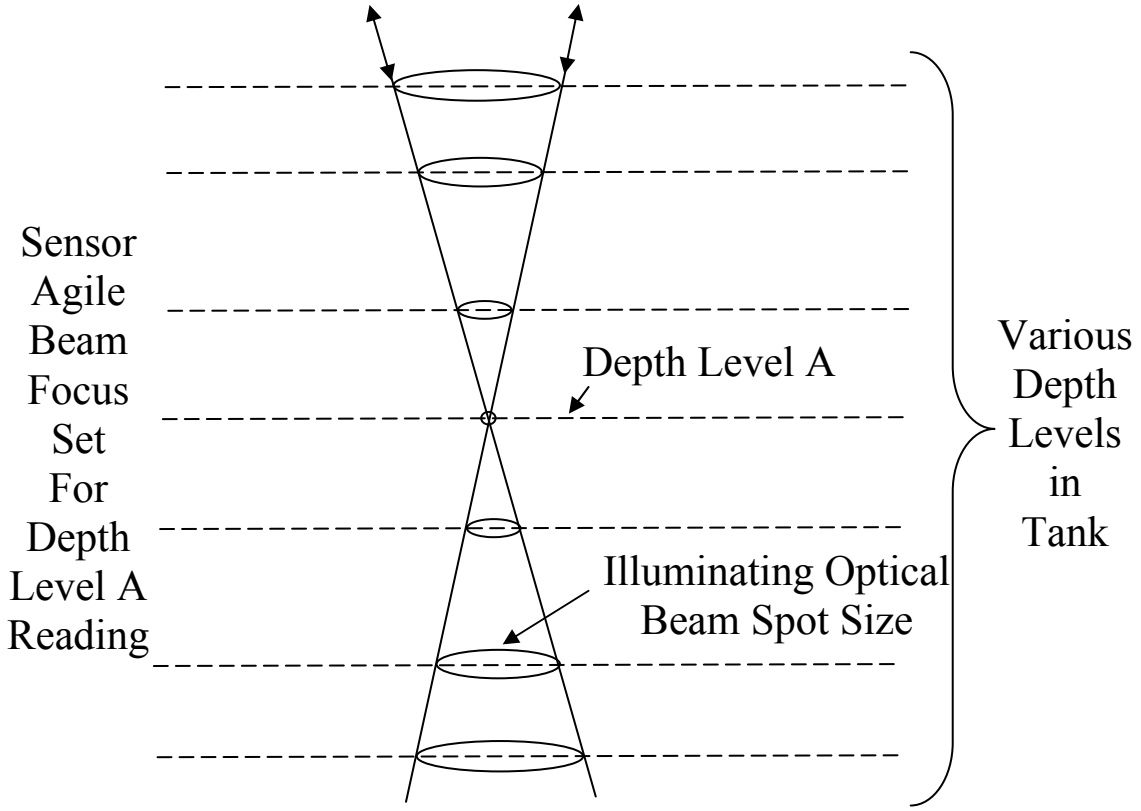

Fig.6.3.2 Sensor laser beam agile focus operation set for liquid depth level A reading corresponding to smallest liquid illumination beam focus spot. Dashed lines represent different liquid depth levels.

The liquid level sensing via the transceiver module is implemented by changing the ECVFL applied control signal. This action in-turn changes the focal length F of the ECVFL that is swept across different values that result in various spot sizes on the plane of the LUT surface. As shown in Fig.6.3.2, the best focus condition is achieved when the optical beam falling on the liquid forms a minimum spot or a minimum beam waist at the

plane of the liquid surface, in this case liquid depth level A. This best focus observation is governed by the imaging condition between the virtual object point P and the surface plane of the LUT given by:

$$D_T = D_S F /(D_S - F). \quad (1)$$

As shown in Fig.1(a), D_T is the total distance from the ECVFL plane to the surface plane of the liquid, i.e., $D_T = D_1 + D_L + D_3$ while D_S is the distance of point P from the ECVFL. The point P position is determined using the known laser beam divergence half angle θ and the known beam radius H at the ECVFL as using geometry:

$$D_S \approx H/\theta. \quad (2)$$

As D_H the tank height and D_1 and D_3 are fixed, D_T can be determined from Eqn.1 leading to a value for D_L. Next one finds the liquid level $D_2 = D_H - D_L$ as changing liquid levels implies a changing D_L. Note that each distinct liquid level D_2 in a given tank would require the ECVFL to be adjusted to a different focal length F in order to form the minimum spot on the liquid surface as viewed by the on-axis CCD or the off-axis camera. Thus by simply noting the ECVFL drive signal value (or the equivalent F) that provided the smallest spot on the liquid level and using a stored calibration table of liquid level versus ECVFL F value, one determines the liquid level in the tank.

In order to reduce the transceiver module size in Fig.5.3.2, a spherical lens S having a focal length F_S is placed between the BS and the CCD. This ensures that the minimum spots still form simultaneously at the CCD and the liquid surface but with a smaller L_4 distance. Without S, the CCD must be placed at a longer distance D_S from the ECVFL plane to ensure that minimum spots get imaged at both the CCD and the liquid surface planes. The distance L_4 needed for the transceiver design is computed in the following way. S is placed at a distance of $L_2 + L_3$ from the ECVFL plane. Therefore the converging rays falling on S can be thought to have converged due to a focal length F_V virtual lens present before S. The distance L_4 is the effective focal length of a two lens (i.e., S and the virtual lens) system with zero inter-lens distance. Hence, using the standard formula for two cascaded lenses one gets:

$$L_4 = \frac{F_V F_S}{(F_V + F_S)}. \quad (3)$$

Given that the ECVFL is controlled by voltage V control, the resolution of liquid level measurement depends on the smallest voltage step that is achievable with a particular voltage controller. The derivative of D_T with respect to the F is calculated from Eq.1 and it is given by:

$$\frac{dD_T}{dF} = \frac{D_S^2}{(D_S - F)^2}. \quad (4)$$

Therefore the liquid level measurement step is given by:

$$\Delta D_T(V) \approx \frac{dD_T}{dF}\Delta F(V) = \frac{D_S^2}{(D_S - F)^2}\Delta F(V). \quad (5)$$

The focal length step ΔF depends on the regime of operation of the applied voltage and therefore it is a function of V. The dynamic range of liquid level measurement depends on the range of the focal lengths that the ECVFL can be tuned to as well as the degree of

collimation of the laser. Note that better laser beam collimation would result in an increased dynamic range of the proposed sensor.

Using Eq.1 and Eq.2, one can write:

$$D_T = \frac{H \times F}{(H - F\theta)}. \tag{6}$$

The sensor dynamic range R is then given by:

$$R = D_{TMax} - D_{TMin} = H\left(\frac{F_{Max}}{(H - F_{Max}\theta)} - \frac{F_{Min}}{(H - F_{Min}\theta)}\right). \tag{7}$$

The minimum F_{Min} and maximum F_{Max} values for the tunable F depend on the type and make of the ECVFL. The radius of the optical beam H at the ECVFL plane should be less than the radius of clear aperture of the ECVFL. The degree of collimation can be adjusted according to the required sensor application and different liquid container depths.

The percentage measurement resolution R_δ is given by:

$$R_\delta = \frac{\Delta D_T}{D_T} = \frac{(D_S - F)D_S + D_S F}{(D_S - F)^2} \times \Delta F \times \frac{D_S - F}{D_S F}, \tag{8}$$

$$\Rightarrow \frac{\Delta D_T}{D_T} = \frac{(D_S - F)D_S + D_S F}{(D_S - F)D_S F} \times \Delta F = \left(\frac{1}{F} + \frac{1}{D_S - F}\right)\Delta F. \tag{9}$$

As can be seen from Eq.9, the percentage resolution varies with the liquid level. The Eq.9 expression depends on the focal length needed to form a minimum beam spot at the liquid surface and this value of F varies with changing liquid levels. Fundamentally, the sensor resolution is limited by the physical effect of the illuminating Gaussian laser beam diffraction for a given F(V), specifically the beam axial (along beam propagation direction) resolution determined by the λ/4 Rayleigh criteria given by $\sim \pm 2\ \lambda\ (F\#)^2$, where F# (F-number) of the ECVFL is equal to F(V)/D and D is the diameter of the ECVFL.

The Fig.5.3.2 sensor is experimentally setup to demonstrate the working principles of the liquid level sensor. Used is a highly attenuated beam from a 10 mW He-Ne LS with λ_L = 632.8 nm and θ = 1.24 mrad. In addition, deployed is a Varioptic (France) Arctic 320 ECVFL with F_{Max} = 21.2 cm at V = 43 V and F_{Min} = 13.07 cm at V = 46 V. The ECVFL has a transmittance of 92% at λ_L. The liquid container has a length $D_2 + D_L = 1\,m$ and diameter 5 cm. A gold mirror M and a glass spherical lens S having a focal length of 10 cm is deployed. For the ECVFL, the applied voltage step is ΔV= 200 mV and the response time is less than 100 ms. H = 0.3275 mm and the distance from the ECVFL to the liquid container top, i.e., $D_1 + D_3 = 25\,cm$. L_1 = 11 cm with $L_1 = L_2 + L_3$ and L_2 = 6 cm and L_3 = 5 cm. For the given experimental conditions, D_S is calculated from Eq. 2 to be 26.43 cm. Therefore F_V is computed as $F_V = D_S - L_1 = 15.43\,cm$ and L_4 comes out to be 6.07 cm. Using Eq.5, the measurement resolution is calculated to be $\leq 0.9\,cm$ with a resolution percentage of < 1.2 %. In the present case with λ= 632.8 nm, F_{Max}(43 V)= 21.2

cm and D = 3.4 mm, the fundamental λ/4 Rayleigh criteria based sensor resolution is ± 4.92 mm. The optical power incident on the liquids is ~ 50 μW.

Liquid levels for three different liquids, namely motor oil, vegetable oil and laundry detergent are measured using the experimental sensor. The liquid optical power reflectivities are measured to be 2.32%, 1.26% and 1.55% for vegetable oil, motor oil and laundry detergent, respectively. Do note that one must operate the CCD in an unsaturated mode to obtain true beam spot size readings. Hence, by using the CCD in its unsaturated mode, any optical power fluctuations within the observed spot size do not affect the spot boundary, thus providing robustness to the liquid level sensor measurement.

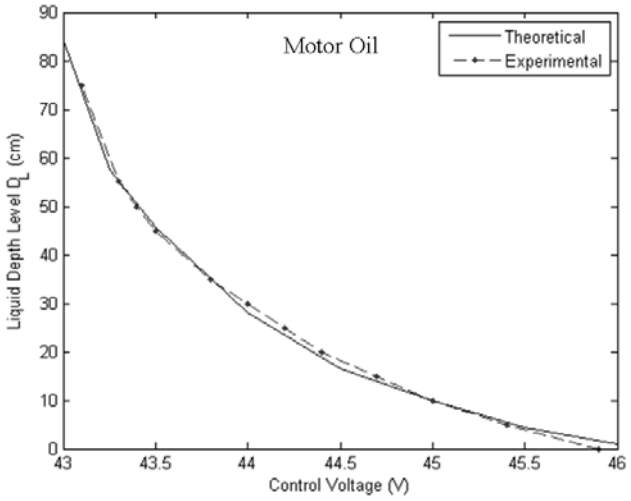

(a)

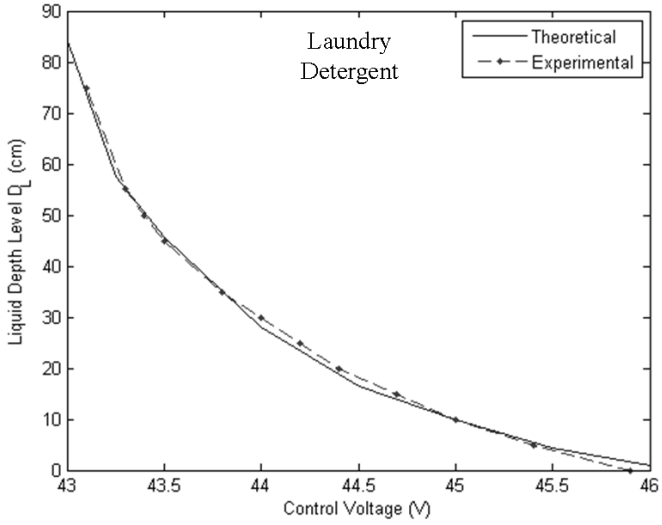

(b)

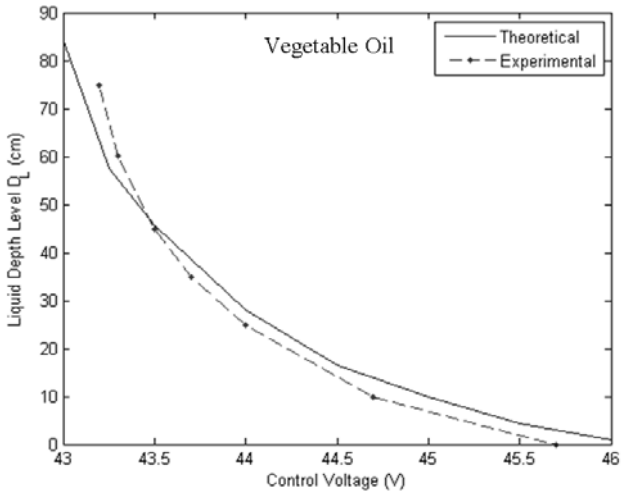

(c)

Fig.6.3.3 Sensor theoretical and experimental plots for the liquid depth level versus the required ECVFL control voltage for formation of minimum beam spot on the liquid surface for (a) motor oil, (b) laundry detergent and (c) vegetable oil.

Note that depending on the designed liquid sensor range and apertures of the optics deployed (i.e., mirror, ECVFL, BS, S, and CCD), one must align the targeting beam accordingly with the surface of the liquid to have full receive beam capture on the CCD. Normal incidence of the beam on the liquid surface is ideally desirable as it retains circular symmetry of the of the ideal circular irradiance distribution of the ideal laser source. Nevertheless, if the laser irradiance is not perfectly symmetrical (e.g., somewhat elliptical such as common with many lasers including laser diodes and the laser used in the experiment), determining the ECVFL voltage when the received beam relative spot size is minimal is more critical to sensor operations versus the actual spot size measurement. Thus, appropriate image processing steps must be performed to compare similar shape beam spots to determine which one has the smallest beam size measure. Depending on the shape of the deployed laser beam, a variety of measurement parameters can be designed and implemented via computer processing.

Plots in Fig.6.3.3a-b compare the theoretical and the experimental applied voltage levels V corresponding to minimum beam spots at the liquid surfaces for different theoretical and deployed liquid levels. As seen from the plots, the theoretical and experimental data are indeed in good agreement for all three test liquids. The measured D_L liquid level depth ranges from 0 cm to 75 cm when V is varied from 43.1 V to 45.9 V. In Fig.6.3.3, the measured control voltage is an average of three voltage data points taken for a given liquid level depth D_L. Note that because the deployed ECVFL focal length response is non-linear with voltage, one should expect a non-linear response for the sensor as is also experimentally confirmed with the results in Fig.6.3.3. The proposed sensor can be operated over a larger dynamic range by increasing the collimation 'θ' of the laser beam. The present sensor design using the raw diverging laser beam can provide a liquid depth

level dynamic range R of 109.44 cm. This full dynamic range can be completely utilized when the ECVFL is in close proximity to the window of the liquid tank. In the existing laboratory setup, the liquid lens is placed 25 cm away from the liquid tank entrance and therefore ~ 84 cm of dynamic range is available for liquid depth sensing for the experimental sensor. Note that the theoretical versus experimental data curve fits are better for the motor oil and detergent liquids versus the vegetable oil. This is because the motor oil and detergent liquids have a higher viscosity than vegetable oil and laboratory environment vibrations have a stronger effect on the lower viscosity liquid surface optical quality.

7. Conclusion:

7.1 Part 1 of Program

Conducted experiments and calculations show that at temperatures greater than about 550 ^{o}C, the TOC of single crystal 6H-SiC changes a minimal amount and essentially becomes constant at about 8 x 10^{-5} / ^{o}C. In effect, the optical power cycles have near constant periods as temperature exceeds about 550 ^{o}C. **C**onducted experiments and calculations also show that the instantaneous temporal response of a 400 micron thick 1 cm x 1 cm square single crystal SiC chip when subjected to a conductive temperature step function of 90 deg-C peak value is under 1/30 seconds. Given the 1 mm diameter conductive heat tip placed on the chip, ~ 16 seconds are required to reach the steady state 90 deg-C temperature of the heat tip from the 25 deg-C room temperature setting. Approximately the same time (~ 17 seconds) is required for the chip to cool down to steady state room temperature by simply using convection cooling, indicating a reversible and repeatable heat/cool refractive index change process for the observed temperature range. A design and assembly study has been conducted to realize a temperature sensor network design using the developed all-SiC temperature probe technology. Experimental results show the robustness of the sensor network to mechanical misalignments of the probe assembly that can cause sensor malfunction. Turbine rig test raw sensor data, including thermal shock on flame ignition has been initially analyzed and compared to Thermo-Couple (TC) temperature readings. The conducted analysis indicates that the TC temperature reading temporal response is similar to the demonstrated single crystal 6H-SiC temperature sensing probe.

7.2 Part 2 of Program

Proposed and demonstrated is a novel temperature sensing method using an all-Silicon Carbide (SiC) probe that combines wavelength-tuned signal processing for coarse measurements and classical Fabry-Perot (FP) etalon peak shift for fine measurements. This method gives direct unambiguous temperature measurements with a high temperature resolution over a wide temperature range. Specifically, temperature measurements from room temperature to 1000^{o}C are experimentally demonstrated with an estimated resolution varying from 0.66 ^{o}C at room temperature to 0.12 ^{o}C at 1000 ^{o}C.
Also proposed and demonstrated is the first extreme environment temperature sensor using Blackbody (BB) radiation of a high temperature material optical chip for coarse temperature measurement and classical Fabry-Perot (FP) laser interferometry via the same chip for fine temperature measurement. Such a hybrid design sensor can be used to

accurately measure temperatures in excess of 750 ^{o}C such as needed for gas turbines in power plants. The proposed sensor is designed and demonstrated using an all-Silicon Carbide (SiC) probe for temperatures from 795 °C to 1077 °C with an estimated average measurement resolution of 0.1 °C.

7.3 Part 3 of Program

A modified optical level measurement sensor design has been proposed towards realization of an all-SiC sensor technology for pressure measurements based on remote laser beam distance measurements. A basic distance sensor has been demonstrated for motions around 100 cm. An opto-fluidic Electronically Controlled Variable Focus Lens (ECVFL) is used to change the spatial intensity profile of the low power optical beam falling on the liquid surface. By observing, tuning and measuring the liquid surface reflected intensity profile to reach its smallest size, the liquid level is determined through a beam spot size versus ECVFL focal length calibration table. Using a 50 microWatt 632.8 nm laser wavelength liquid illuminating beam, a proof-of-concept sensor is tested using engine oil, vegetable oil, and detergent fluid with measured liquid levels over a 75 cm range. This non-contact Radio Frequency (RF) modulation-free sensor is particularly suited for hazardous fluids in window-accessed sealed containers including liquid carrying vessels in Electromagnetic Interference (EMI) rich environments.

The **overall program conclusion** is that all-SiC optical sensor technology has the fundamental material science as well as the engineering innovations to form a strong basis for extreme environment sensing in next generation gas turbines for efficient and clean power plant design. Further engineering studies are required for testing optimal sensor designs in extreme environments with longer-term tests in mind to prove deployable parts reliability and accuracy.

8. References

1. N. A. Riza and S. A. Reza, “Non-Contact Distance Sensor using Spatial Signal Processing," Optics Letters, Vol.34, No.4, pp.434-436, Feb.15, 2009.
2. M. Sheikh and N. A. Riza, “Direct Measurement High Resolution Wide Range Extreme Temperature Optical Sensor using an all-Silicon Carbide Probe,” Optics Letters, May 1, 2009.
3. N. A. Riza, M. Sheikh, and F. Perez, “Hybrid Wireless-Wired Optical Sensor for Extreme Temperature Measurement in Next Generation Energy Efficient Gas Turbines,” *ASME Journal of Engineering for Gas Turbines and Power,* vol. 132, May 2010.
4. N. A. Riza and M. Sheikh, “All-Silicon Carbide Hybrid Wireless-Wired Optics Temperature Sensor Network Basic Design Engineering for Power Plant Gas Turbines,” International Journal of Optomechatronics, Vol.4, No.1, Jan-March, Taylor & Francis, pp. 83-91, 2010.
5. N. A. Riza and M. Sheikh, “Silicon Carbide-based High Resolution Extreme Environment Hybrid Design Temperature Sensor using Optical Pyrometry and Laser Interferometry,” *IEEE Sensors J.,* , Vol.10, No.2, Feb. 2010.
6. S. A. Reza and N. A. Riza, “Agile Lensing-based Non-Contact Liquid Level Optical Sensor for Extreme Environments,” Optics Communications, Vol.283, pp.3391-3397, 2010.